Supporting Information

Tungsten Single Atoms Incorporated in Cobalt Spinel Oxide for Highly Efficient Electrocatalytic Oxygen Evolution in Acid

Jing Cao[1,2], Dezheng Zhang[1,2], Bianqing Ren[1,2], Ping Song[1*], Weilin Xu[1,2*]

1 State Key Laboratory of Electroanalytical Chemistry, Changchun Institute of Applied Chemistry, Chinese Academy of Sciences, Changchun 130022, PR China

2 University of Science and Technology of China, Hefei 230026, PR China

Corresponding author: Ping Song (songping@ciac.ac.cn), Weilin Xu (weilinxu@ciac.ac.cn)

Methods

Materials

Tungstic acid (H_2WO_4, solid, 99%), Cobaltous nitrate hexahydrate (($Co(NO_3)_2$• $6H_2O$, solid, 99%) were purchased from Aladdin. hydrogen peroxide (H_2O_2, liquid, 30%) and sulfuric acid (H_2SO_4, liquid, ≥ 96%) were purchased from Xilong scientific. Carbon paper (HGP-H-90, EC-TP1-060T) was purchased from Toray.

Catalysts synthesis

The preparation of W-Co_3O_4 was based on a thermal decomposition method, as described previously[1]. In a typical synthesis, 0.15 g H_2WO_4 was first dissolved in 6 mL H_2O_2 and heated at 80 ℃ to obtain a homogeneous solution (0.1 mol /L H_2WO_4). Add 100 uL 0.1 mol /L H_2WO_4 to 450 uL of 0.3 mol/L $Co(NO_3)_2$ solution and mix well. Then, a 1cm*2 cm hydrophilic carbon paper (HGP-H-90) was placed in the center of a 1.5cm *2.5 cm hydrophobic carbon paper (EC-TP1-060T), the W-Co mixed solution was dropped onto the exposed hydrophilic carbon paper and calcined on at 450 °C in the air (or 350 ℃ or 500 °C as specifically discussed) for 2 h in a muffle furnace to transform into oxides. The resultant electrode was sonicated for 10 s to remove any loosely connected particles and rinsed with Milli-Q ultra-pure water. Finally, the electrodes were dried for 12 hours at 40 °C in an oven. Co_3O_4, WO_3, and W-Co_3O_4 with different amounts of W dopant were prepared also following the same procedure by thermal decomposition of $Co(NO_3)_2$ (0.3 mol/L, 450 uL), H_2WO_4 (0.1 mol/L, 450 uL), two W-Co mixed solution (120 uL H_2WO_4 + 450 uL $Co(NO_3)_2$, 80 uL H_2WO_4 + 450 uL $Co(NO_3)_2$).

The synthesis process of Mo-Co_3O_4, Nb-Co_3O_4, Ni-Co_3O_4, and Mn-Co_3O_4 were the same as that of W-Co_3O_4, the precursor salts used were NbCl5, $(NH_4)_2MoO_4$, $Ni(NO_3)_2$, and $Mn(NO_3)_2$, respectively.

The synthesis process of W-MnO_2, MnO_2 were the same as that of W-Co_3O_4, and only need to replace $Co(NO_3)_2$ to $Mn(NO_3)_2$.

The preparation of WO_3/Co_3O_4: 0.015g of H_2WO_4 was first dissolved in 6 mL of H_2O

and heated at 50 °C to achieve complete dissolution. The WO_3/Co_3O_4 catalyst was synthesised by adding 150 uL of 0.9 mol/L $Co(NO_3)_2$ into 1000 uL of H_2WO_4 solution, and then following the procedure for the preparation of W-Co_3O_4.

Characterizations

Power X-ray diffractometer (PXRD) was performed on a Rigaku Smartlab diffractometer with Cu Kα radiation. Transmission electron microscopy (TEM), High-Angle Annular Dark Field-Scan transmission electron microscopy (HADDF-STEM), Element mapping analysis and electronic energy loss spectroscopy (EELS) were performed on Cs-TEM FEI Titan G2 at 300 kV. Electron paramagnetic resonance (EPR) spectra were conducted on a Bruker A300. Raman spectra were collected with a LabRAM HR laser Raman analyzer (Horiba/Jobin Yvon, Longjumeau) outfitted with a frequency-doubled Nd: YAG 532.1 nm laser. Inductively coupled plasma optical emission spectroscopy (ICP-OES, Thermo Scientific iCAP 7400) was used to determine the content of W, Co of W-Co_3O_4, and the dissolution of metal of electrolyte after the stability test.

XAFS measurements

XAFS spectra at the W L_3-edge energy were collected at the BL14W1 beamlines at the Shanghai Synchrotron Radiation Facility (Si (111)), The XAFS spectra were recorded at room temperature using a 4-channel Silicon Drift Detector (SDD) Bruker 5040. XAFS spectra at the Co *K*-edge were collected was carried out using the *Rapid XAFS* 2M (Anhui Absorption Spectroscopy Analysis Instrument Co., Ltd.) by transmission mode. The energy was calibrated by the absorption edge of W foil and Co foil, respectively. The XAFS spectra of these standard samples were recorded in transmission mode. The XAFS raw data were extracted the data and fitted the profiles by using Athena and Artemis. The theoretical scattering amplitudes, phase shifts, and photoelectron mean free path for all paths were calculated in the IFEFFIT package using a Hanning window. The data were fitted in R-space using theoretical models built based on the

XRD-derived crystal structure.

Differential electrochemical mass spectrometric measurements.

In situ DEMS experiments was performed on an in situ differential electrochemical mass spectrometer provided by Linglu Instruments (Shanghai) Co. Ltd. A typical test was carried out in a three-electrode cell with N_2 saturated 0.5 M H_2SO_4 as electrolyte. Firstly, the W-Co_3O_4 and Co_3O_4 samples were labelled with ^{18}O isotopes in 0.5 M H_2SO_4 solution at 1.5 V for 10 minutes. The electrodes were repeatedly cleaned with $H_2{}^{16}O$ and dried in an oven to eliminate any remaining $H_2{}^{18}O$. To eliminate the electrode of adsorbed ^{18}O species, cyclic voltammetry was performed between 0.6 and 1.2 V at 50 mV s^{-1} before to DEMS measurement. After these operations, the samples were subjected to an in situ DEMS measurement with an applied potential.

Electrochemical measurements

All electrochemical measurements were carried out in a three-electrode cell on CHI 760E. The materials deposited on the carbon paper were directly used as the working electrode, and a carbon rod and a Hg/Hg_2SO_4 ((saturated K_2SO_4) was used as the counter electrode and the reference electrode. O_2 saturated 0.5 M H_2SO_4 was used as an electrolyte. In this work, all potentials measured are converted to the reversible hydrogen electrode (RHE) and following Eq (1):

$$E\ (RHE) = E\ (Hg/Hg_2SO_4) + 0.675\ V \qquad \text{Eq (1)}$$

Here, 0.675 V is the value to use a reversible hydrogen electrode to calibrate the Hg/Hg_2SO_4 in 0.5 M H_2SO_4. Linear sweep voltammetry (LSV) curves and Cyclic voltammetry (CV) were obtained at a scan rate of 5 mV/s in 0.5 M H_2SO_4. The geometric area (0.25 cm^2) of the electrode exposed to the electrolyte solutions was used to calculate the current density. Based on the resistance values acquired using electrochemical impedance spectroscopy (EIS), the ohmic resistance was adjusted following the electrochemical tests. EIS was collected in the frequency range from 100 kHz to 100 mHz. The stability of catalysts was evaluated by chronopotentiometry at 10 mA/cm^2.

Calculation of the electrochemically active surface area (ECSA)

The ECSA of catalysts was obtained from the electrochemical double-layer capacitance (C_{dl}) according to Eq (2):

$$\mathrm{ECSA} = \mathrm{RfS} = \frac{\mathrm{Cdl}}{\mathrm{Cs}}\mathrm{S} \qquad \text{Eq(2)}$$

C_{dl} was measured from double-layer charging curves using cyclic voltammetry in a non-Faradaic region with a scan rate from 2 to 12 mV s^{-1}. S denotes the smooth metal electrode's real surface area, which was generally equal to the geometric area of the glassy carbon electrode (S = 0.25 cm^2). In this work, according to previous research, the specific capacitance (Cs) for a flat surface was used to be 60 µF cm^{-2} to estimate the ECSA.[2]

PEMWE tests

For electrolyzer tests, a self-made cell was used as the PEMWE device and a cation exchange membrane (Nafion 115) as the membrane electrolyte. The MEAs were prepared by using the Pt/C (40 %, JM) as the cathode catalyst coated membrane. The cathode ink was prepared by ultrasonically blending the catalyst with Nafion solution, DI water, and isopropanol, followed by air-sprayed directly onto the Nafion membrane of 4 cm^2 areas. The Pt loading at the cathode was fixed at 0.8 mg/cm^2 (Ionomer-to-catalyst ratio was 0.4). The dried Nafion membrane with cathode catalysts was placed in 0.5 M H_2SO_4 solution at 80 ℃ for 30 min to activate the proton conduction channel, and then heated in deionised water at 80 ℃ for 30 min, and rinsed with deionised water for several times. The anode was prepared by W-Co_3O_4 thermal composition on Pt-coated (2 um) Ti felt, and W-Co_3O_4 loading at the anode was 8 mg/cm^2. The anode and the cathode catalyst coated membrane were hot pressed at 300 pounds for 2 min at 120 ℃. To construct the PEM electrolyzers, for cathode, the carbon paper was used as the porous transport layers (PTL). For anode, Pt-coated Ti felt was used as the PTL. The assembly pressure of the fixture is set to 4 N m. The PEM electrolyzers were operated at 50 ºC. The reactant of the constructed PEM electrolyzer is MilliQ water, which is supplied through peristaltic

pump circulation, and the flow rate is set as 25 mL min^{-1}.

Energy efficiency calculation: $\text{Energy efficiency} = \frac{1.23\ V}{E_{cell}}$ Eq (3)

where 1.23 V is the theoretical energy of the products, E_{cell} is the cell voltage (V) required to deliver a current density of 1 A cm^{-2}.

Hydrogen production cost= energy consumption × electricity bill

energy consumption is calculated at 1 A cm^{-2}, and the electricity bill is obtained from the previous reports ($ 0.02/Kw h).

$$\text{energy consumption} = \frac{E_{cell} * I_{cell}}{m_{H2}} \text{t} \qquad \text{Eq}(4)$$

where I_{cell} is the delivered current (A), t is the operation time (h), m_{H2} is the mass of hydrogen produced in a t duration, which can be calculated by Faraday's laws of electrolysis: $m_{H2} = \frac{I_{cell} * t}{Z * F} * M_{H2}$ z=2 is the number of electrons transferred to produce one hydrogen molecule , M_{H2} relative molecular mass (2 g mol^{-1}).

Calculation of the activation energy

The electrochemical measurements of the catalysts were carried out in 0.5 M H_2SO_4 solution at various temperatures (25-65 ℃) to get the apparent activation energy (E_{app}) and the apparent pre-exponential factor (A_{app}) for the acidic OER. For heterogeneous electrocatalytic reactions, the current density can be expressed from E_{app} and A_{app} in the Arrhenius Eq (5)[3-5]:

$$\text{j} = \text{A}_{app}\exp\left(\frac{-E_{APP}}{RT}\right) \qquad \text{Eq (5)}$$

R is the ideal gas constant (8.314 J K^{-1} mol^{-1}), E_{app} can be fitted the slope of the Arrhenius plot using Eq. (6)

$$\left|\frac{\partial(\log_{10} j)}{\partial(1/T)}\right| = -\frac{E_{app}}{2.303R} \qquad \text{Eq. (6)}$$

while the intercept of $\log_{10}j$ vs. 1/T plot is the logarithm of A_{app}.

Computational details

First-principles DFT within the generalized gradient approximation (GGA) using the

Perdew-Burke-Ernzerhof (PBE) formation were employed the plane-wave code Vienna ab-initio simulation package (VASP).[6-8] The energy cut-off of the plane-wave basis was set at 500 eV for plane-wave expansion. Projector-augmented wave pseudo-potential was used to describe the ionic cores and take valence electrons. The energy difference between iterations was converged until it was smaller than 10^{-6} eV. The optimized (311) plane was adopted as the model for surface reaction pathways. Co_3O_4 (311) was constructed by cutting the bulk Co_3O_4 alone 311 directions. W-Co_3O_4 structure was constructed by replaced one Co atom on the surface of Co_3O_4 according to the XAS fitting data. This slab was separated by a 15 Å vacuum layer in the z direction between the slab and its periodic images. During structural optimizations of the surface models, a 3×2×1 gamma-point centered k-point grid for Brillouin zone was used. The d-band center was calculated by the average of the integral of d-band pDOS information. The Gibbs Free energy was calculated based on the conventional four-step electro-proton coupled OER mechanism proposed by Nørskov.[9]

$$2H_2O\,(l) + * \longrightarrow H_2O + HO^* + H^+ + e^- \qquad \Delta G_1$$

$$H_2O\,(l) + HO^* + e^- + H^+ \longrightarrow H_2O + O^* + 2(H^+ + e^-) \qquad \Delta G_2$$

$$H_2O\,(l) + O^* + 2(H^+ + e^-) \longrightarrow HOO^* + 3(H^+ + e^-) \qquad \Delta G_3$$

$$HOO^* + 3(H^+ + e^-) \longrightarrow O_2(g) + 4(H^+ + e^-) \qquad \Delta G_4$$

The overpotential (η) is defined as:

$$\eta = (\max\{\Delta G_1, \Delta G_2, \Delta G_3, \Delta G_4\} - 1.23eV)/e$$

Both free energy profiles were computed on the Ir and Co sites in samples. The overpotentials used were 0 and 1.23 V vs. RHE, respectively. Considering the contributions from zero-point energies and entropies, the Gibbs free energies of adsorption are defined as

$$G_{ads} = E_{ads} + \Delta ZPE - T\Delta S$$

The zero-point energies and entropies of the adsorbates were computed from

vibrational frequency calculations, in which only the adsorbate vibrational modes were computed explicitly, while the catalyst was fixed. The zero-point energies and entropies of gas phase molecules were obtained from NIST database.

Figures

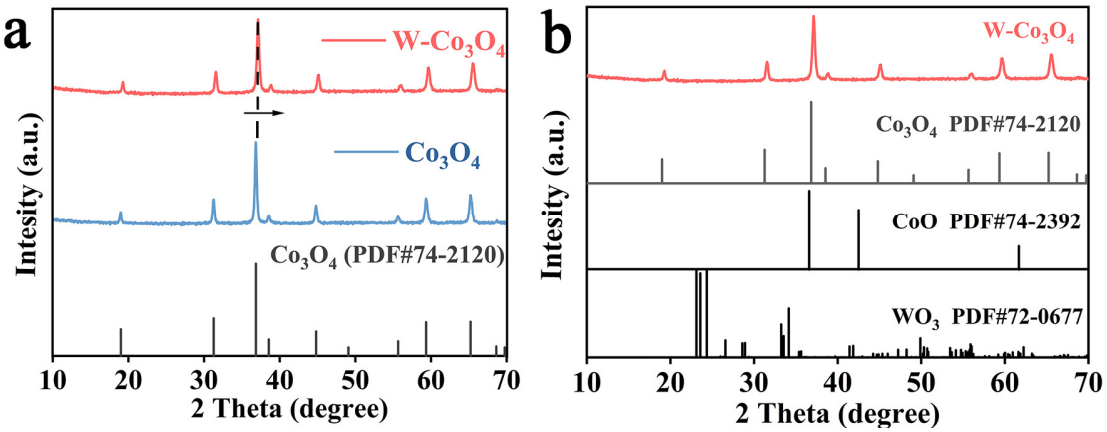

Figure S1. (a-b) Powder XRD patterns of W-Co_3O_4, Co_3O_4 and standard of Co_3O_4, CoO, and WO_3. The result demonstrated that W-Co_3O_4 did not exist CoO and WO_3 phases.

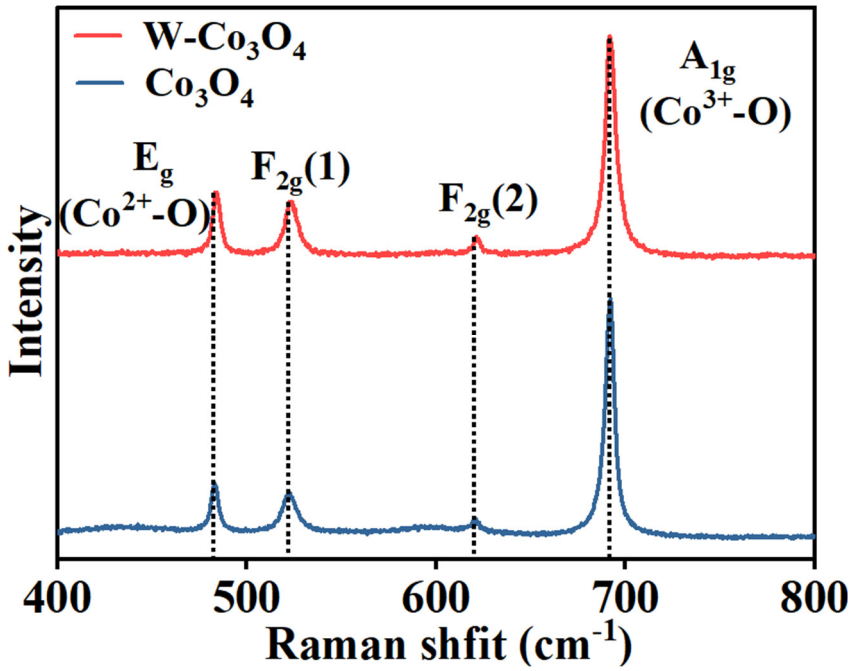

Figure S2. Raman spectra of W-Co_3O_4, Co_3O_4. In the Raman spectra, the ratio of Co^{2+}/Co^{3+} in the catalysts can be calculated based the ratio of integrated peak intensity associated with Co^{2+}-O vibrations (F_{2g} to that of associated with Co^{3+}-O vibration (A_{1g}). The ratios are higher in W-Co_3O_4 compared to that Co_3O_4, indicating a higher ratio of Co^{2+} to Co^{3+} than Co_3O_4.

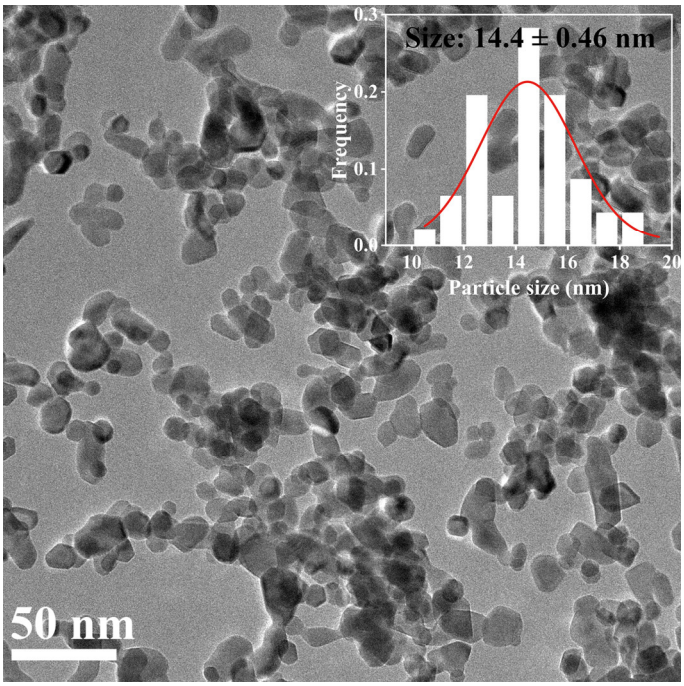

Figure S3. TEM image and particle size distribution of Co_3O_4.

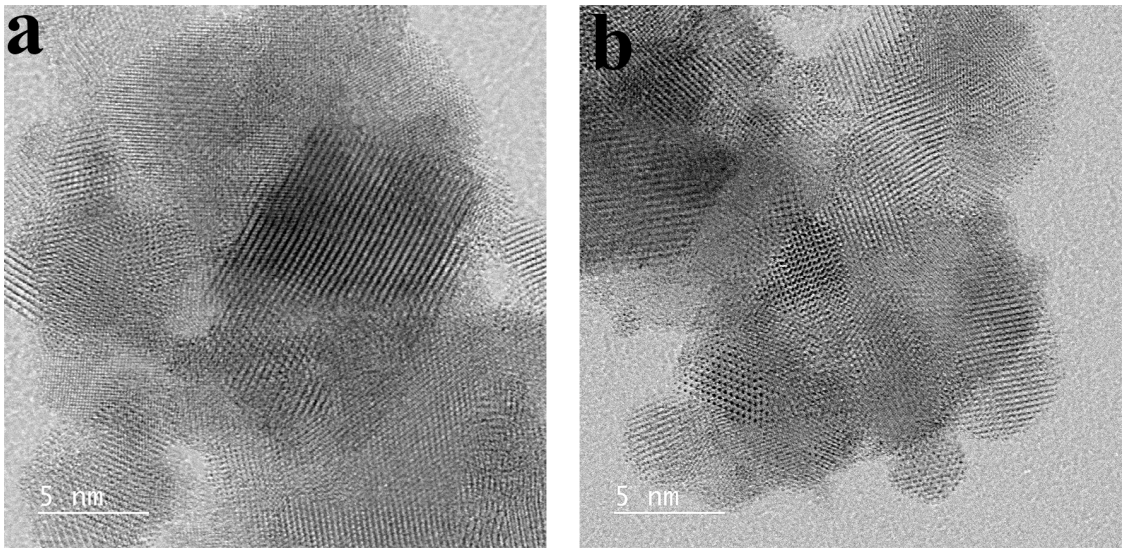

Figure S4. HR-TEM images of Co_3O_4 (a) and W-Co_3O_4 (b).

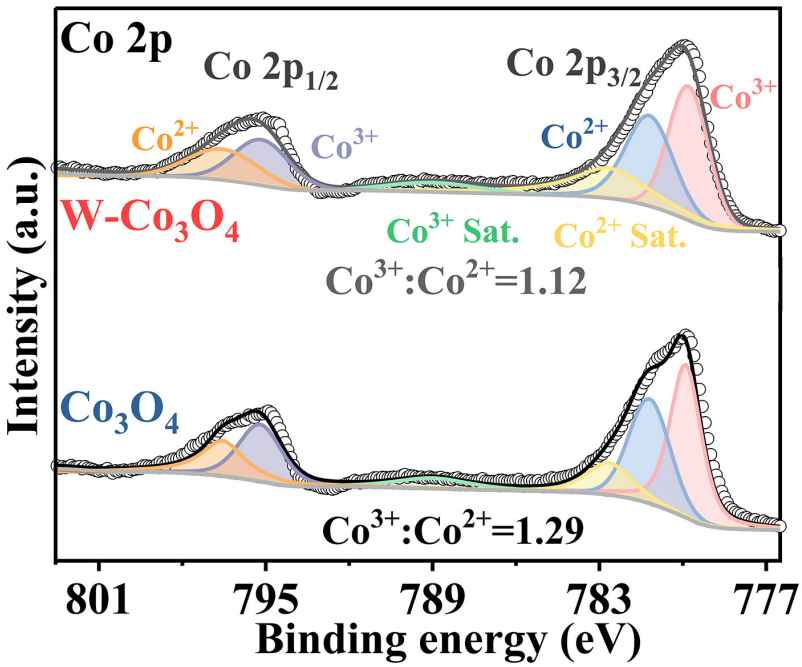

Figure S5. The Co 2p spectra of powder W-Co_3O_4 and Co_3O_4.

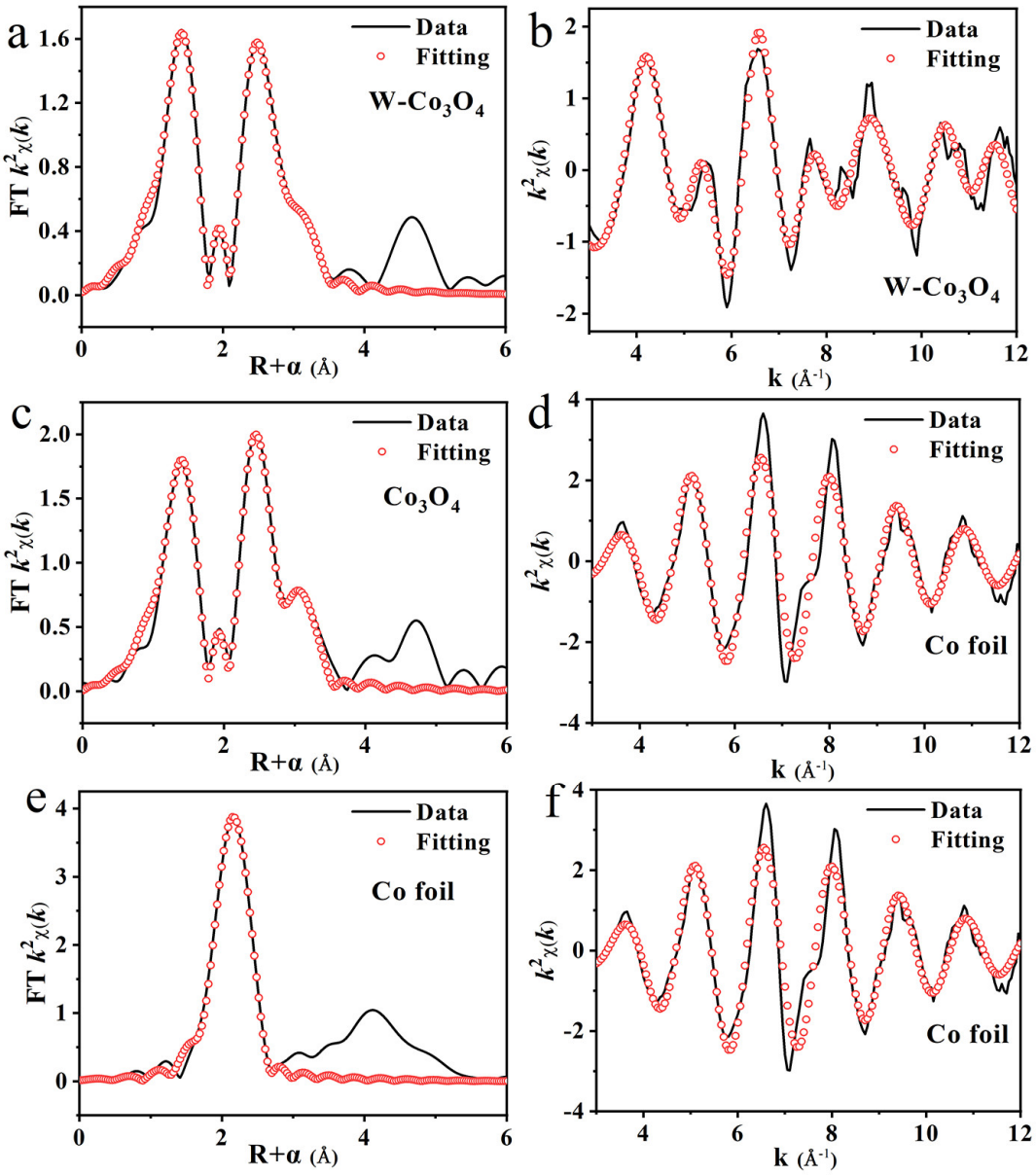

Figure S6. EXAFS fitting. Co K edge EXAFS fitting curves of W-Co_3O_4, Co_3O_4, and Co foil. at (a, c, e) R space and (b, d, f) k space

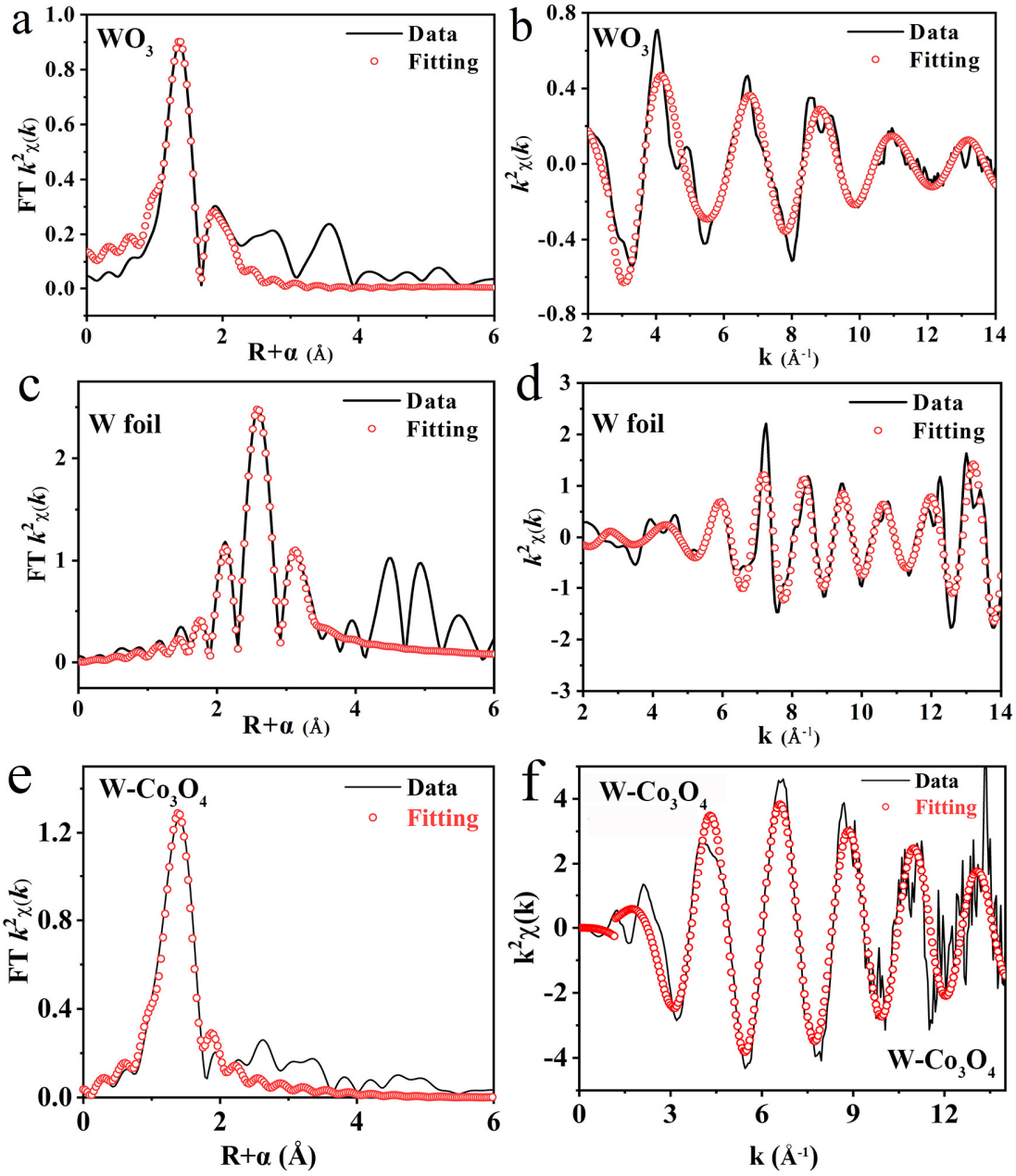

Figure S7. EXAFS fitting. W L_3 edge EXAFS fitting curves of WO_3, W foil, and W-Co_3O_4 at (a, c, e) R space and (b, d, f) k space

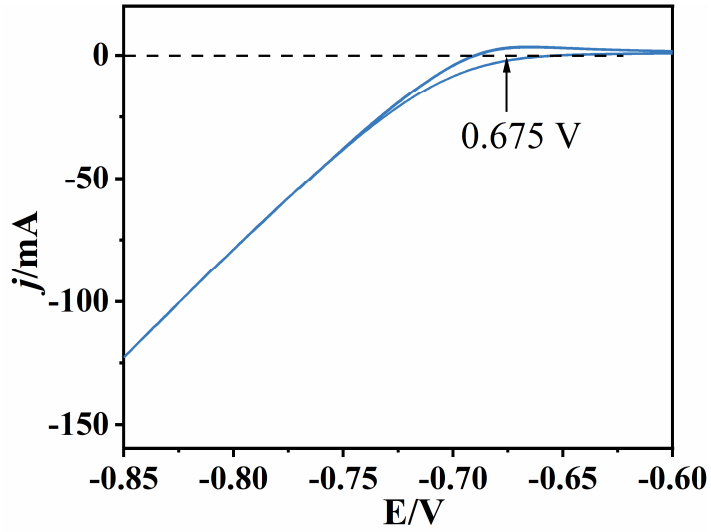

Figure S8. Potential calibration of the Hg/Hg_2SO_4 electrode at 25 °C in H_2-saturated 0.5 M H_2SO_4 solution.

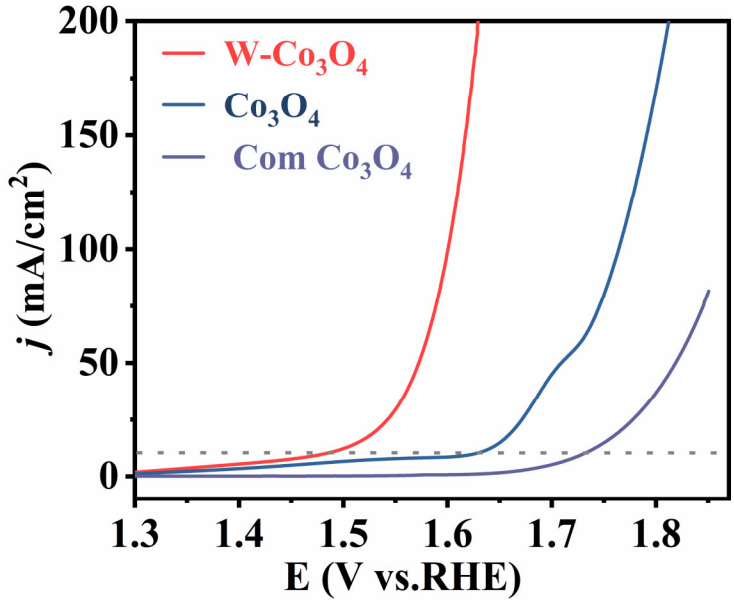

Figure S9. LSV curves of W-Co_3O_4, Co_3O_4, and Com Co_3O_4 in 0.5 M H_2SO_4.

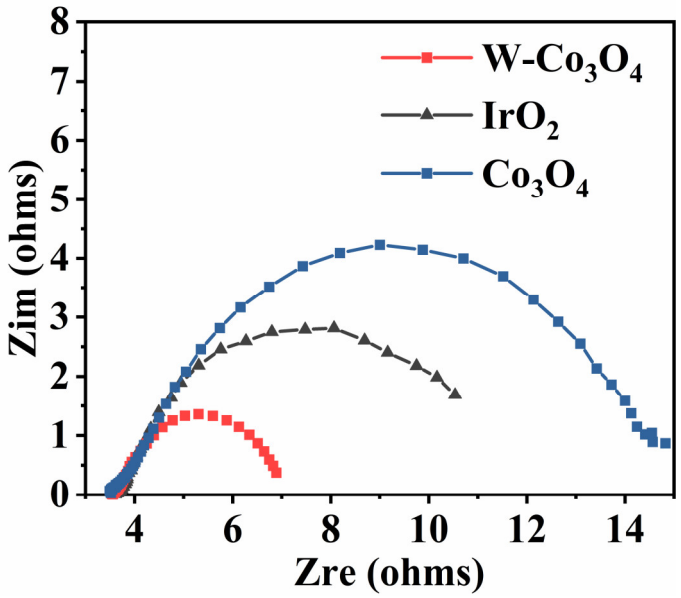

Figure S10. EIS of W-Co_3O_4, IrO_2, and Co_3O_4

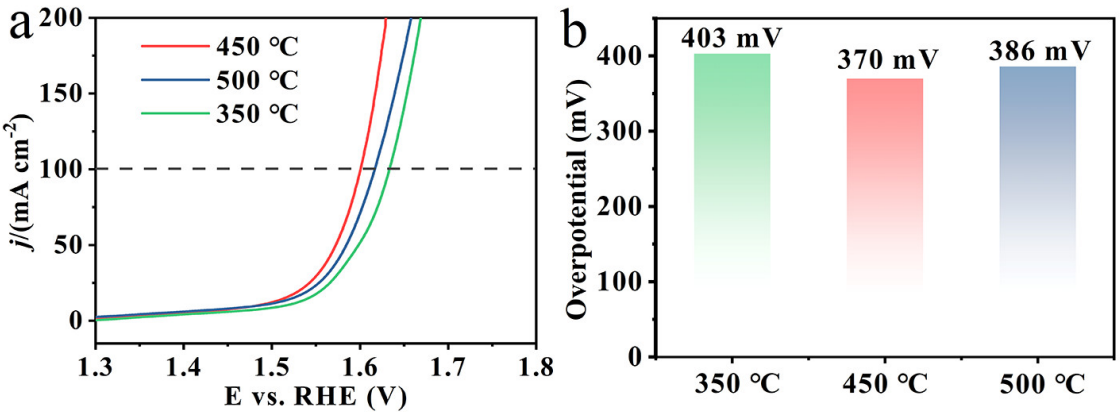

Figure S11. LSV curves (a) and overpotential at 100 mA/cm^2 (b) of the catalysts with different heated temperatures (350, 450, and 500 °C) in the air in 0.5 M H_2SO_4. The results indicated that W-Co_3O_4 with a temperature of 450 °C shows better catalytic activity for OER, compared with catalysts at other temperatures (350, 500 °C), with the overpotential 370 mV at 100 mA/cm^2. It can be seen intuitively that too low or too high temperature is not favorable to the catalytic reaction.

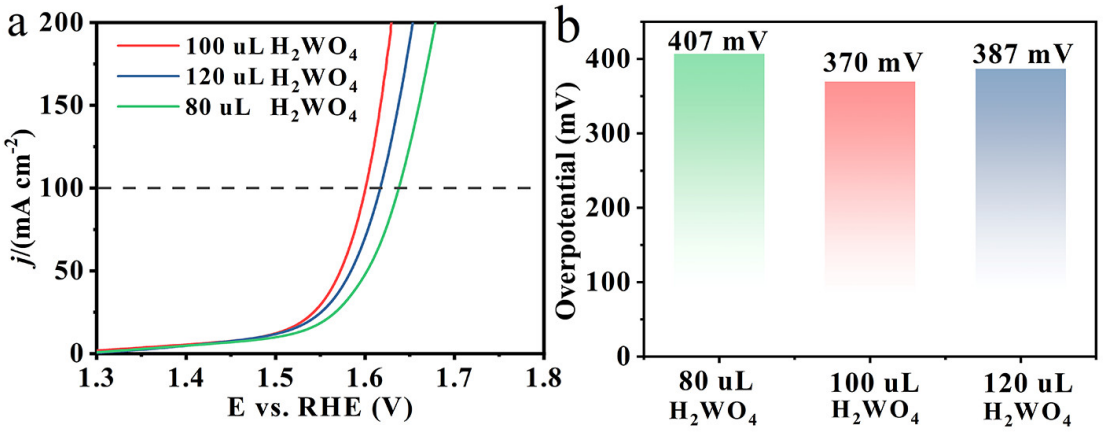

Figure S12. LSV curves (a) and overpotential at 100 mA/cm^2 (b) of the catalysts with different volumes of H_2WO_4 (80, 100, and 120 uL C_{H2WO4}: 0.1 mol/L) and 450 uL 0.3 mol/L $Co(NO_3)_2$ were dropped onto carbon paper and heated 450 ℃ in the air. The results indicated that W-Co_3O_4 with pyrolysis 100 uL H_2WO_4 shows better catalytic activity for OER, compared with catalysts at other W content, with the overpotential 370 mV at 100 mA/cm^2. When the W content of W-Co_3O_4 increased, OER activity decayed. It can be seen intuitively that excessive W loading is not beneficial to the catalytic reaction.

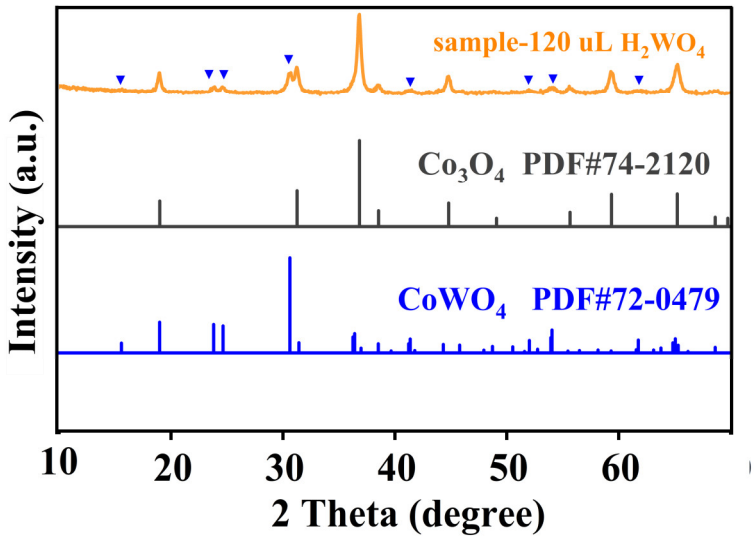

Figure S13. Powder XRD patterns of the sample (120 uL H_2WO_4) and standard of Co_3O_4, $CoWO_4$.

According to the XRD results, the main explanation for the decline in the OER activity of the catalyst with the addition of 120 uL W precursor is the formation of the $CoWO_4$ phase.

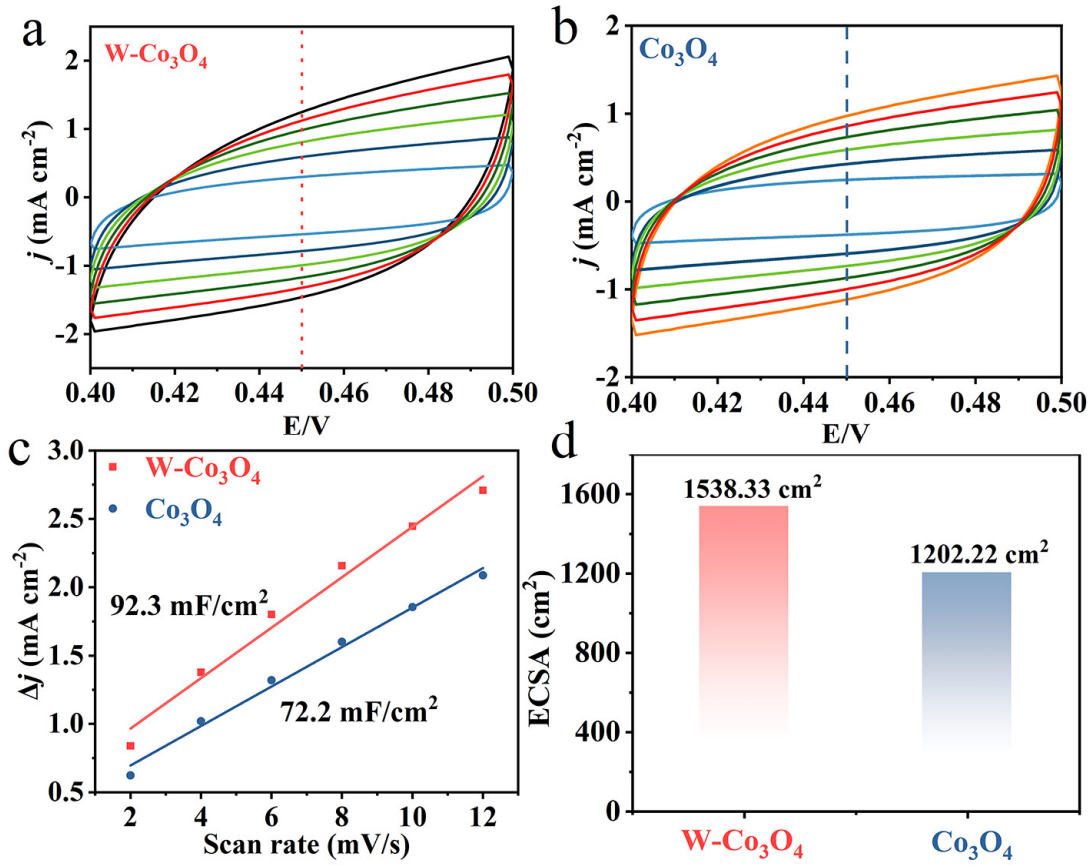

Figure S14. Electrochemical CV scans were recorded for (a) W-Co_3O_4, and (b) Co_3O_4. Scan rates are 2, 4, 6, 8, 10, and 12 mV/s, respectively. (c) Linear fitting of the capacitive currents versus cyclic voltammetry scans for these catalysts at 0.45 V (E vs Hg/Hg_2SO_4). (d) The calculated ECSA values for W-Co_3O_4 and Co_3O_4.

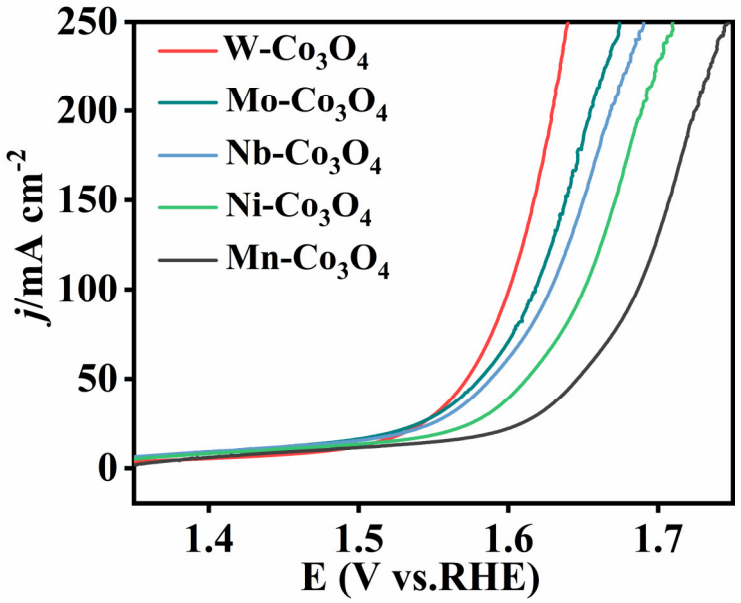

Figure S15. LSV curves of W-Co_3O_4, Mo-Co_3O_4, Nb-Co_3O_4, Ni-Co_3O_4, and Mn-Co_3O_4 in 0.5 M H_2SO_4.

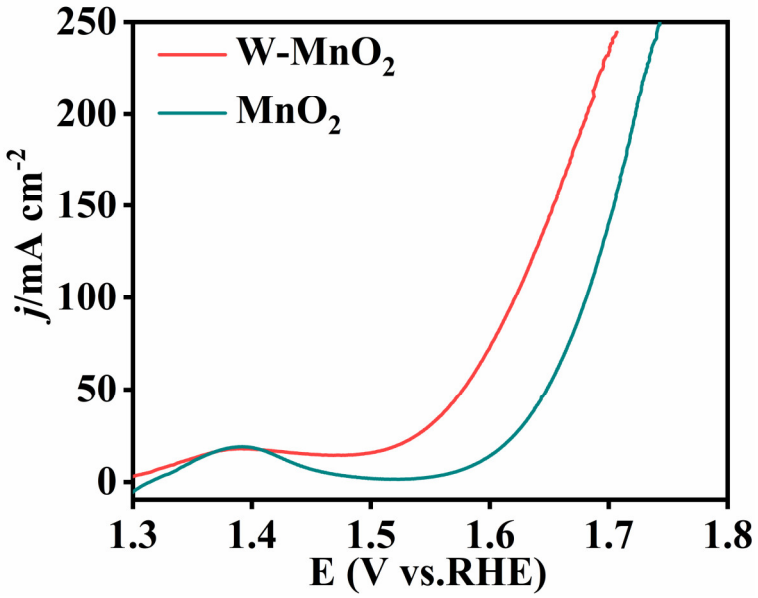

Figure S16. LSV curves of W-MnO_2 and MnO_2 in 0.5 M H_2SO_4.

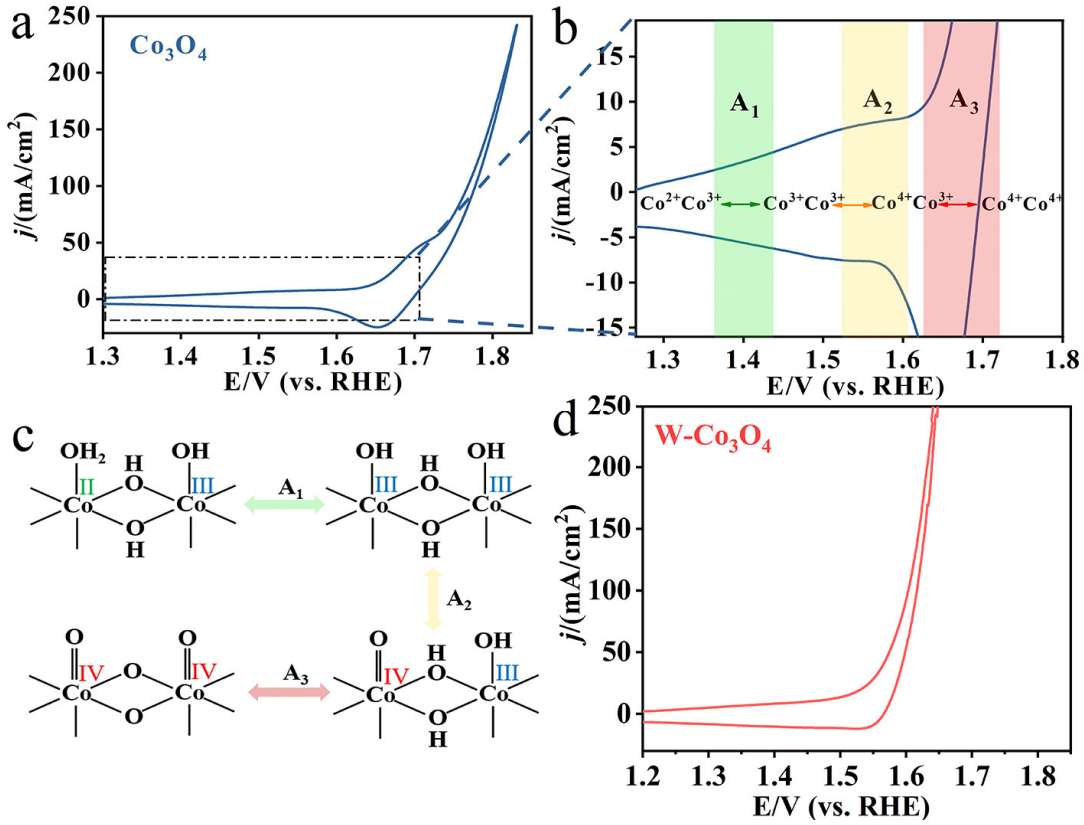

Figure S17. The CV curves of Co_3O_4 (a) and W-Co_3O_4 (d) on carbon paper in 0.5 M H_2SO_4. (b) Magnified CV curve of the Co_3O_4 (a) catalyst that highlights the three pre-OER redox features and the corresponding A_1, A_2, and A_3 cathodic peaks. (c) Structural associated with the three sets of pre-OER redox features (A_1, A_2, and A_3) present in the Co_3O_4 catalyst in acidic media that involve dimeric Co redox centers.

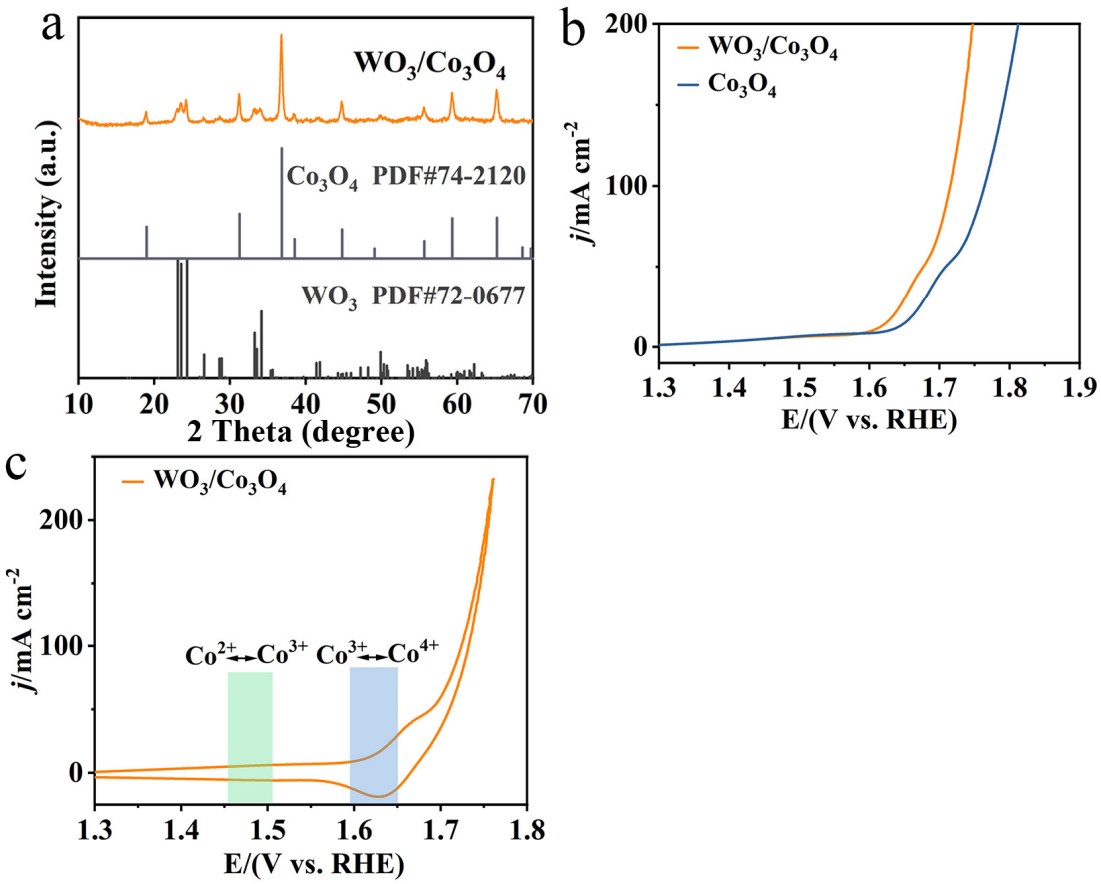

Figure S18. (a) Powder XRD patterns of WO_3/Co_3O_4. (b) LSV curves of WO_3/Co_3O_4 and Co_3O_4. (c) CV curve of WO_3/Co_3O_4.

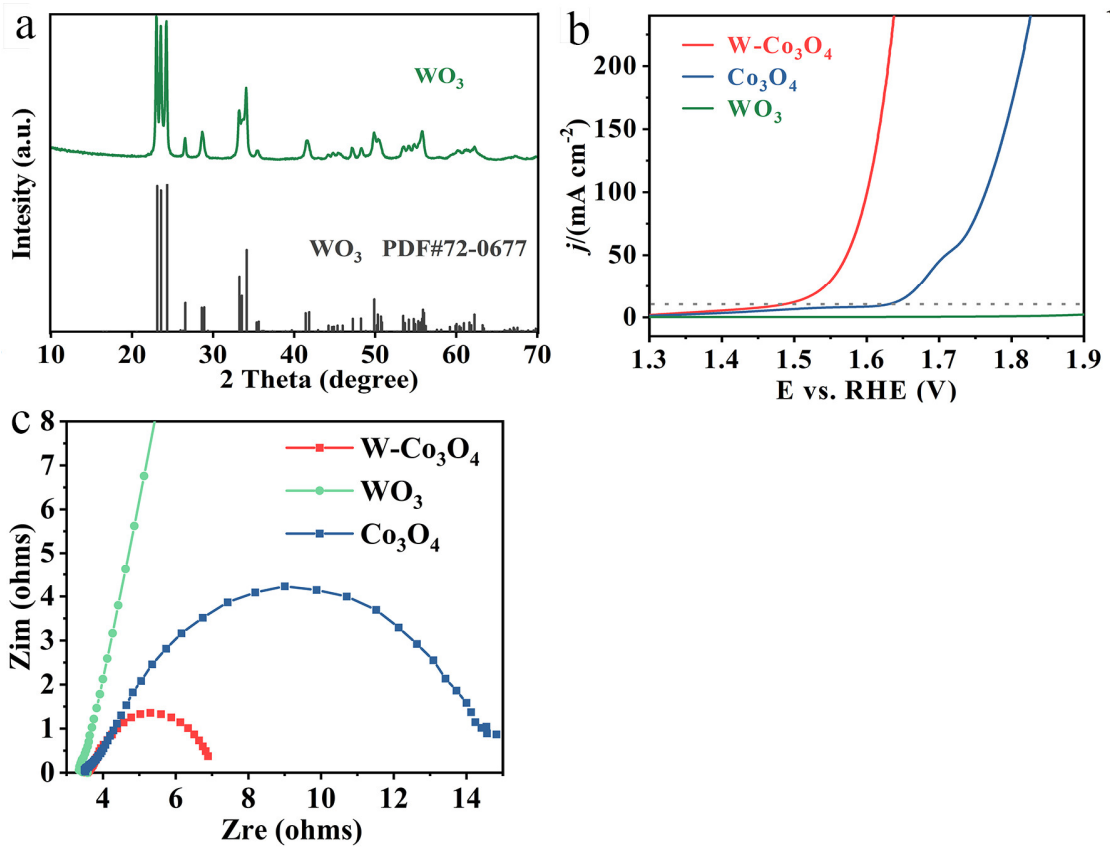

Figure S19. (a) PXRD patterns of WO_3 with the standard of WO_3. (b) LSV curves and EIS (c) of W-Co_3O_4, Co_3O_4, and WO_3. The result indicated that WO_3 did not exhibit OER activity in acid conditions.

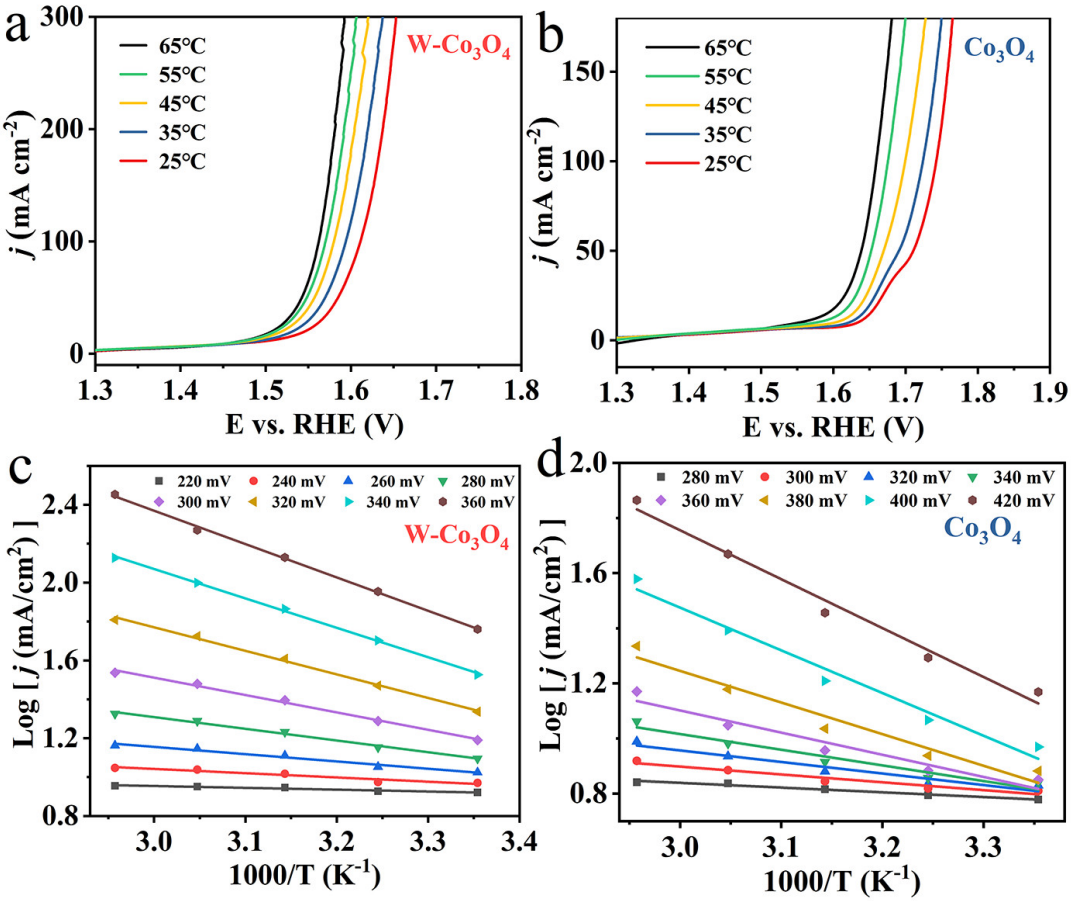

Figure S20. LSV curves of W-Co_3O_4 (a) and Co_3O_4 (b) on carbon paper recorded in 0.5 M H_2SO_4 at different temperatures (25, 35, 45, 55, and 65℃). The apparent activation energy (E_{app}) and pre-exponential factor (A_{app}) of the acidic OER on W-Co_3O_4 (c) and Co_3O_4 (d) were calculated by plotting the logarithm of the catalytic current density versus 1000 times the reciprocal of the temperature (in Kelvin).

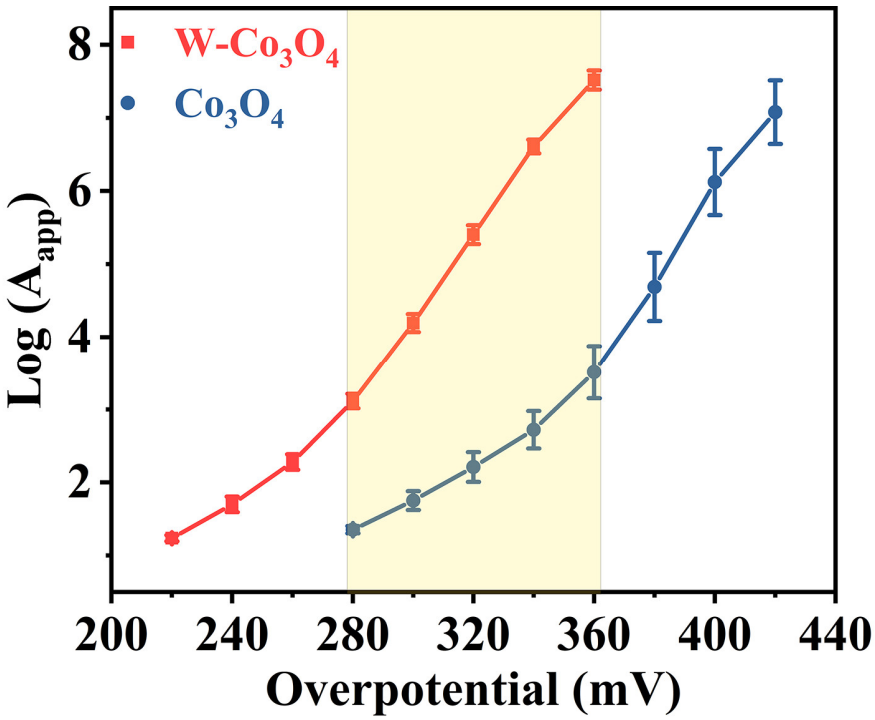

Figure S21. The logarithm of the pre-exponential factor A_{app} was calculated from the intercept during E_{app} extraction for W-Co_3O_4 and Co_3O_4 catalysts at fixed overpotentials using Arrhenius plots. The error bar represents the standard error from fitting.

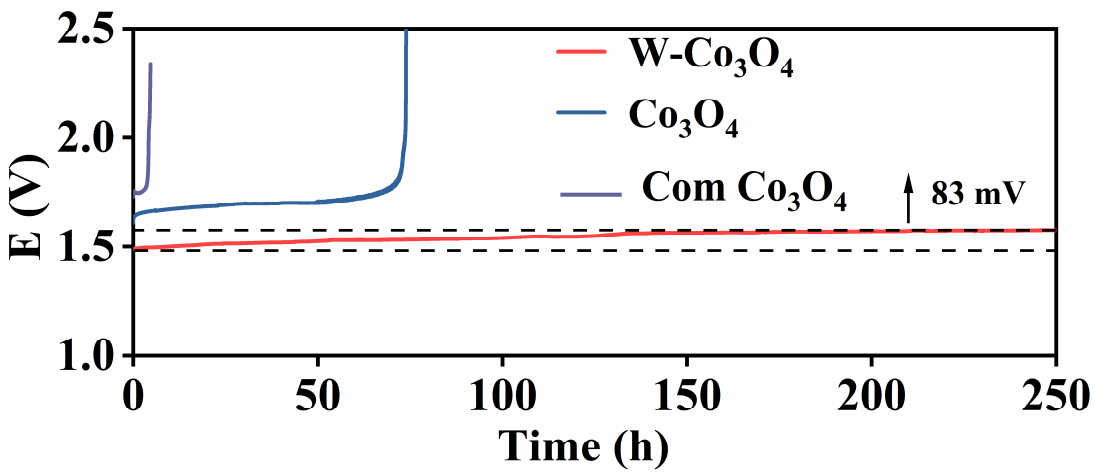

Figure S22. The chronopotentiometry curves of W-Co_3O_4, Co_3O_4, and Com Co_3O_4 at 10 mA/cm^2 in 0.5 M H_2SO_4.

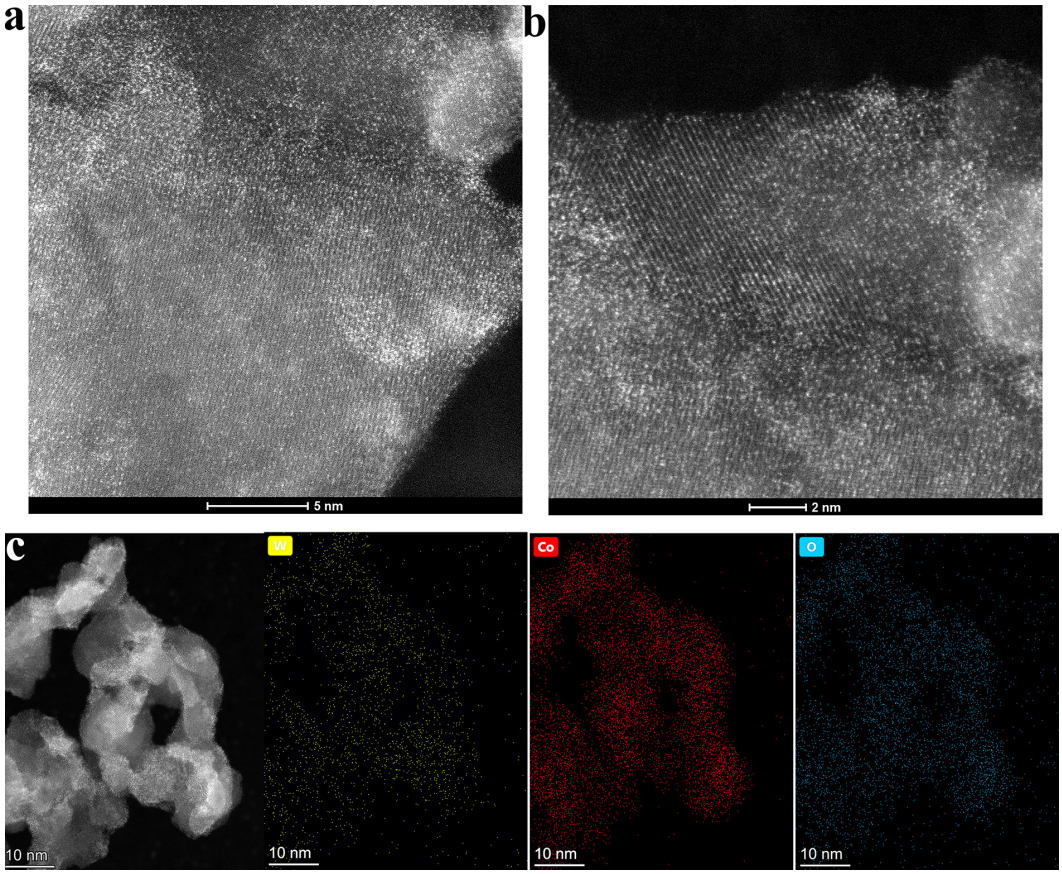

Figure S23. (a-b) The Cs-corrected STEM images of W-Co_3O_4 after OER. (c) The HAADF-STEM image of W-Co_3O_4 after OER and corresponding EDS elemental mappings of W, Co, and O.

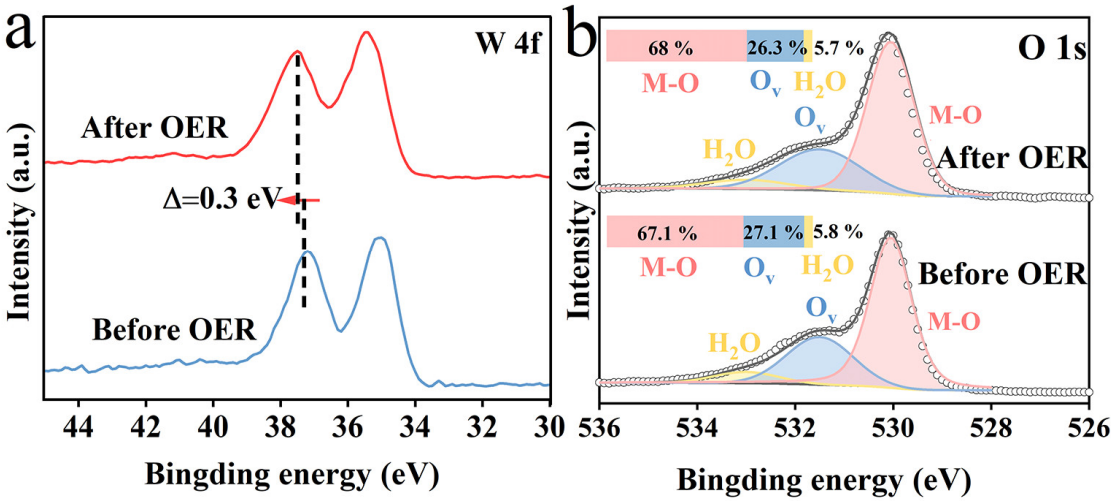

Figure S24. The W 4f and O 1s spectra of W-Co_3O_4 on carbon paper after OER and before OER.

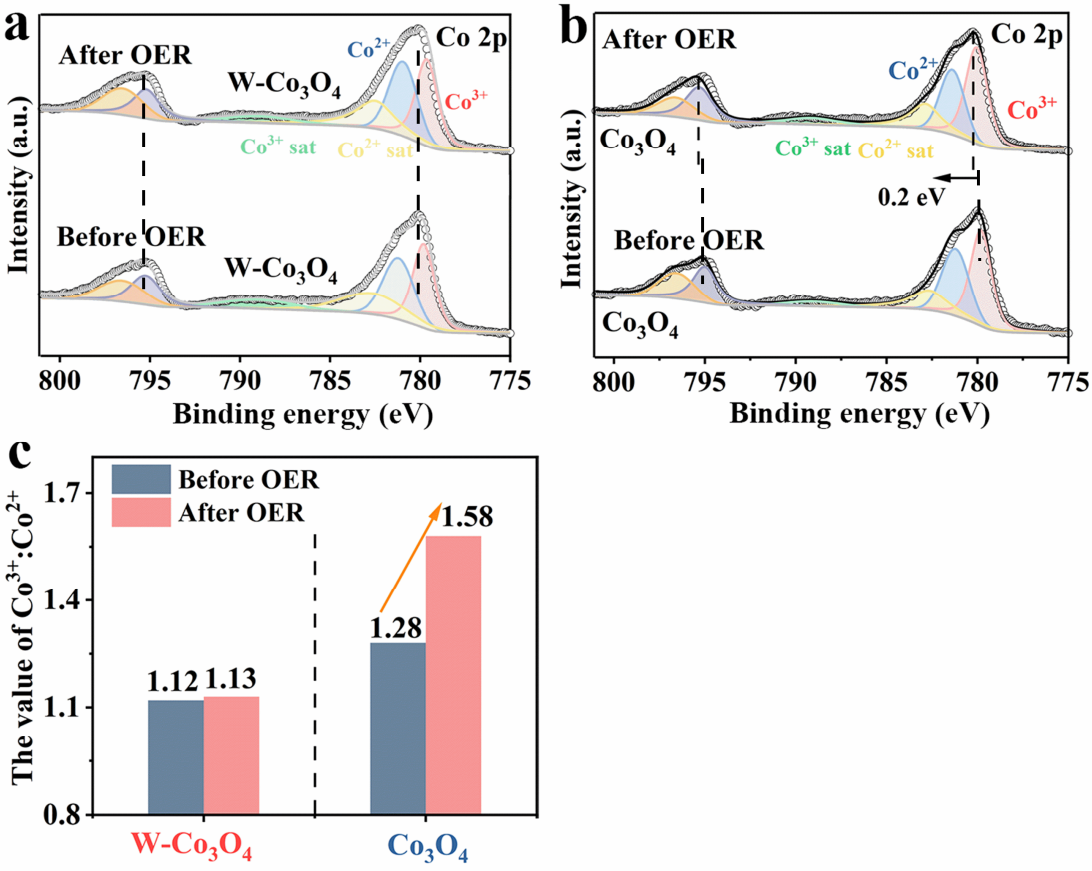

Figure S25. The Co 2p spectra of catalysts on carbon paper after OER and before OER. (a) W-Co_3O_4, (b) Co_3O_4. (c) The XPS fitting results of Co^{3+}: Co^{2+}.

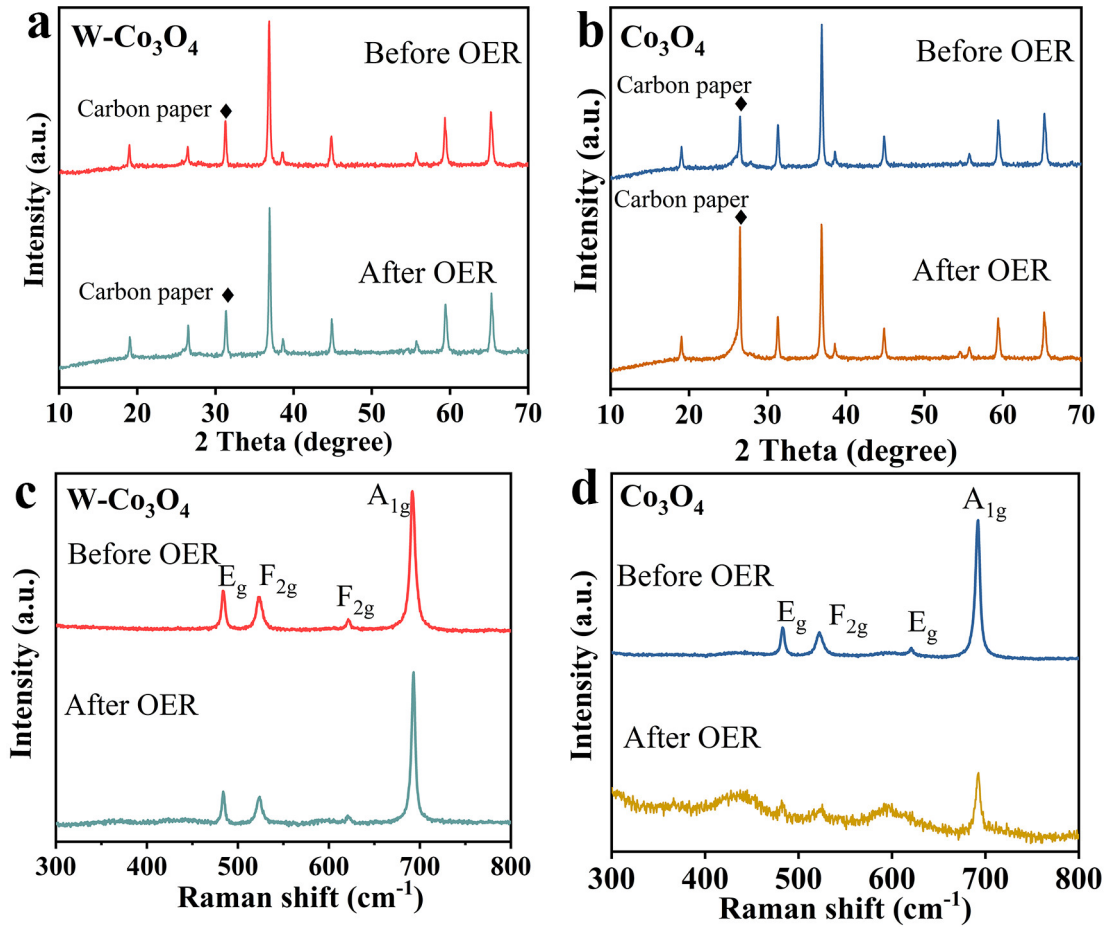

Figure S26. (a-b) XRD patterns of W-Co_3O_4, and Co_3O_4 on carbon paper after OER and before OER. (c-d) Raman spectra of W-Co_3O_4, Co_3O_4 on carbon paper after OER and before OER.

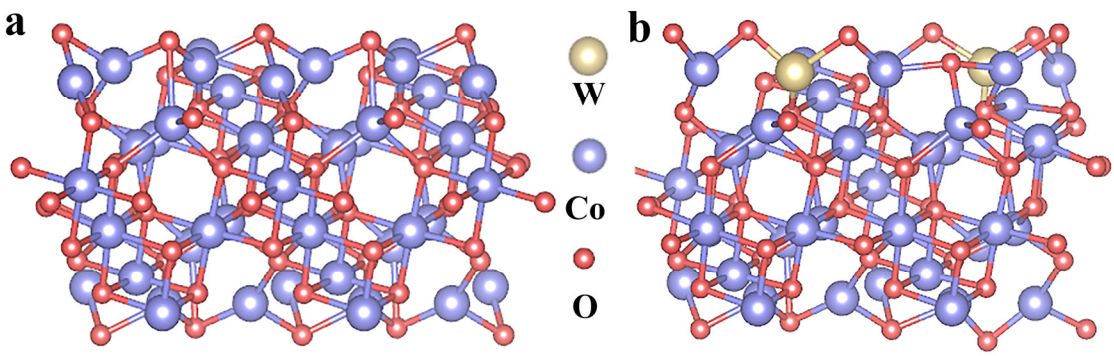

Figure S27. DFT Calculated structures of (a) the Co_3O_4 (311) and W-Co_3O_4 surface.

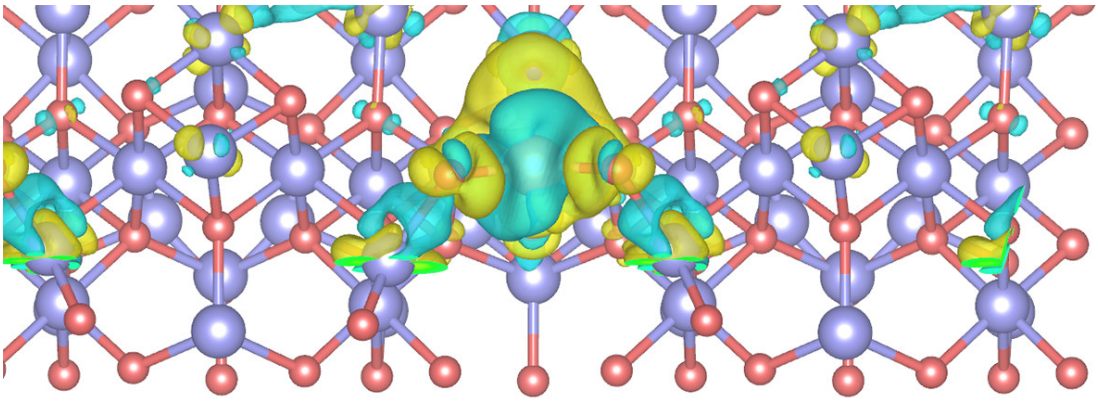

Figure S28. The top panel of charge density difference on W-Co_3O_4.

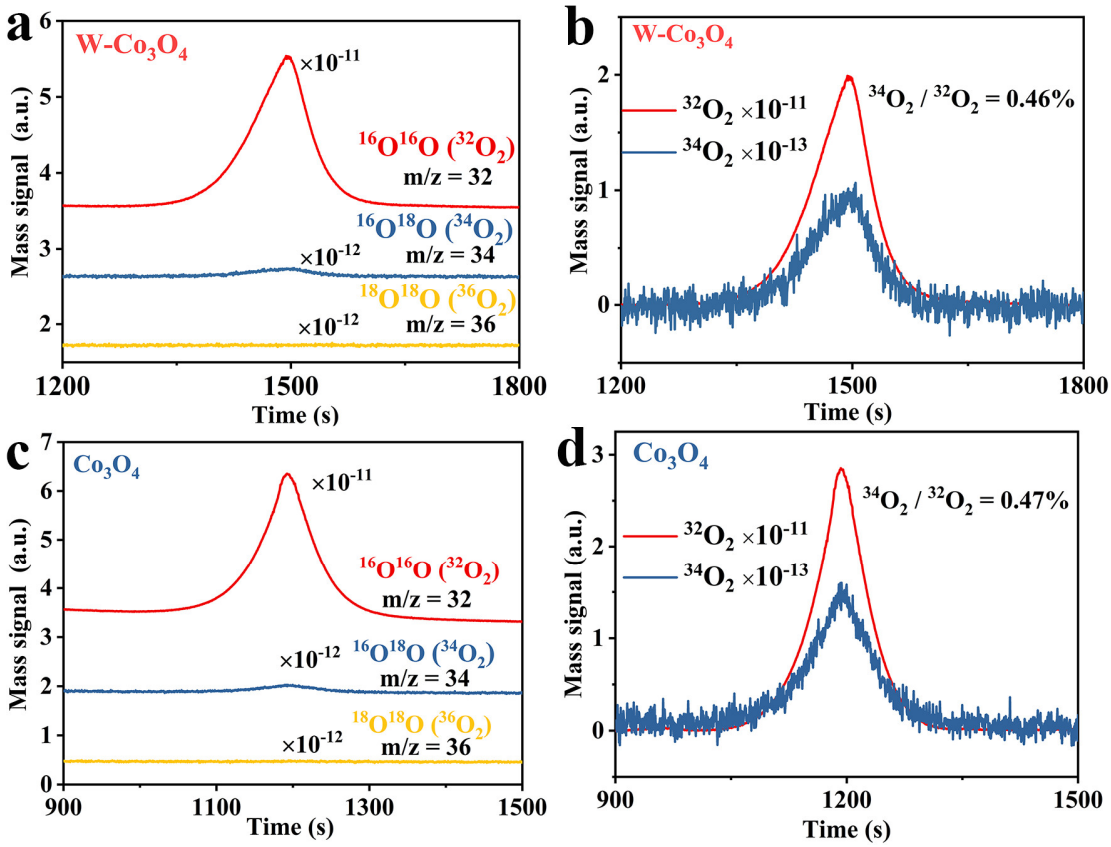

Figure S29. (a) (c) DEMS measurements of $^{16}O^{16}O$, $^{16}O^{18}O$, and $^{18}O^{18}O$ signals from the reaction products for^{18}O-labeled W-Co_3O_4 and Co_3O_4 catalysts in 0.5M H_2SO_4 in $H_2{}^{16}O$. (b) (d) The ratio of $^{34}O_2$ to $^{32}O_2$ for W-Co_3O_4 and Co_3O_4 catalysts.

To validate the occurrence of AEM, we further carried out *in situ* ^{18}O isotope-labeling Differential Electrochemical Mass Spectrometry (DEMS) measurements. The W-Co_3O_4 and Co_3O_4 catalysts were then labeled with ^{18}O isotopes by potentiostatic reaction in ^{18}O-labeled 0.5 M H_2SO_4 electrolyte. As shown in Figure S29a and Figure S29c, the m/z=36 signal was not detected during the OER for W-Co_3O_4 and Co_3O_4 catalysts representing the no presence of $^{36}O_2$($^{18}O^{18}O$) in the gas production, and a minimum amount of m/z=34 signal ($^{16}O^{18}O$) was detected in OER products on both catalysts. By calculating the ratio of ^{34}O to O_2 (Figure S29b and Figure S29d), we found that attributable to the natural isotopic abundance (~0.2%) of ^{18}O in water. **This claim is supported that W-Co_3O_4 and Co_3O_4 follow the AEM by DEMS results.**

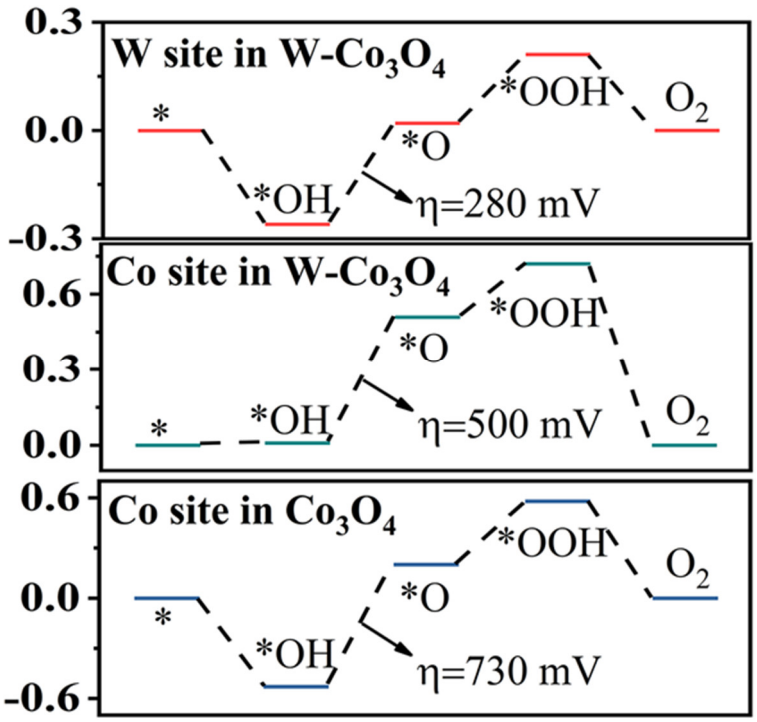

Figure S30. The Gibbs free energy graphs of the four-electron OER process on the W sites and Co sites of these catalysts at 1.23 V vs. RHE applied overpotentials, respectively.

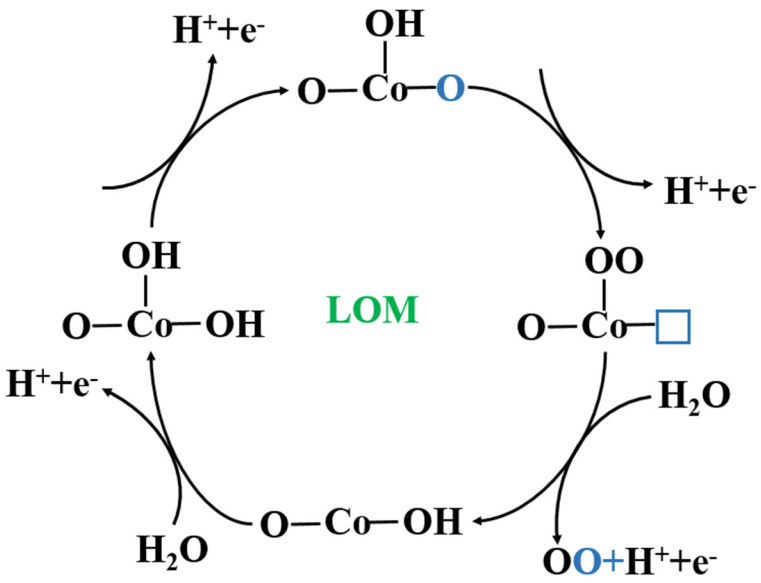

Figure S31. The illustration of LOM mechanism.

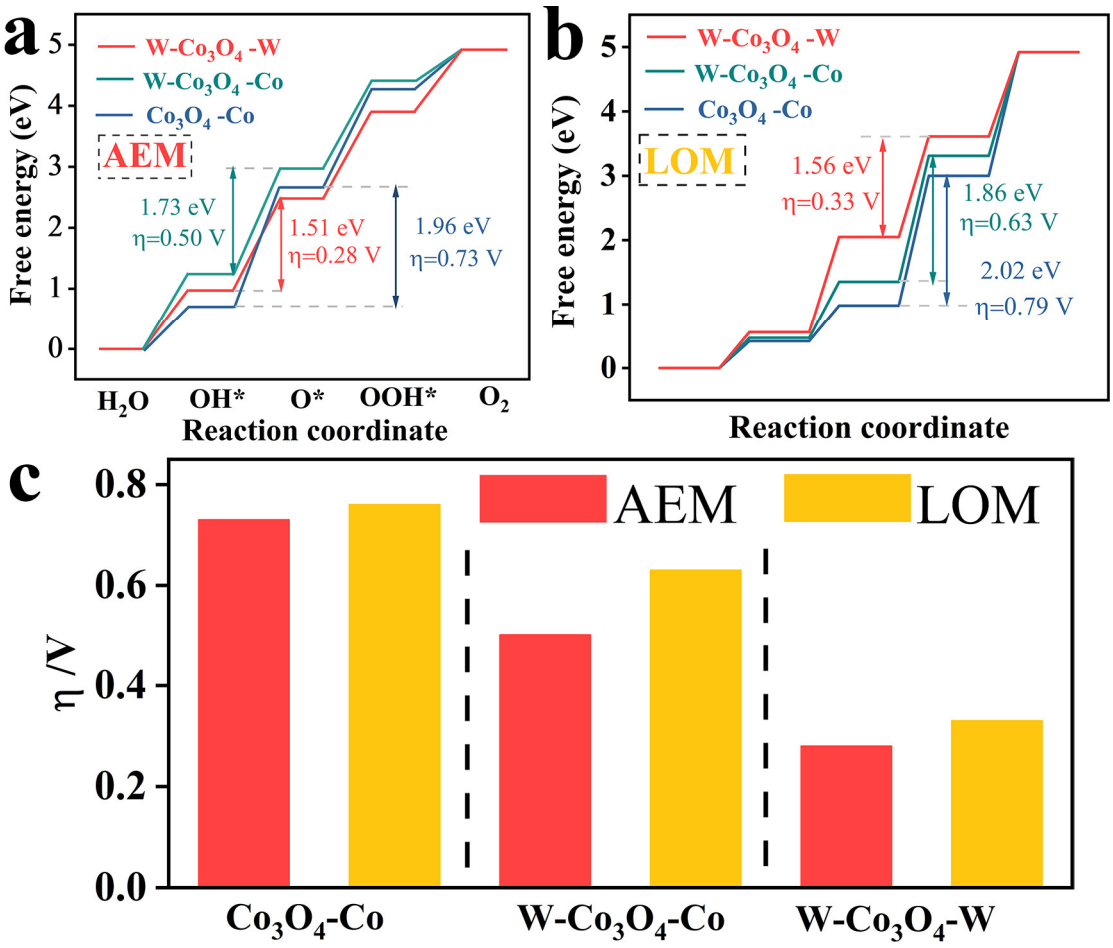

Figure S32. (a) The reaction free energy diagrams for OER at 0 V vs. RHE on Co_3O_4 (311)-Co, W-Co_3O_4 (311)-Co, and W-Co_3O_4 (311)-W by the AEM. (b) The reaction free energy diagrams for OER at 0 V vs. RHE on Co_3O_4 (311)-Co, W-Co_3O_4 (311)-Co, and W-Co_3O_4 (311)-W by the LOM. (c) The theoretical overpotential of Co_3O_4 (311)-Co, W-Co_3O_4 (311)-Co, and W-Co_3O_4 (311)-W by the AEM and LOM.

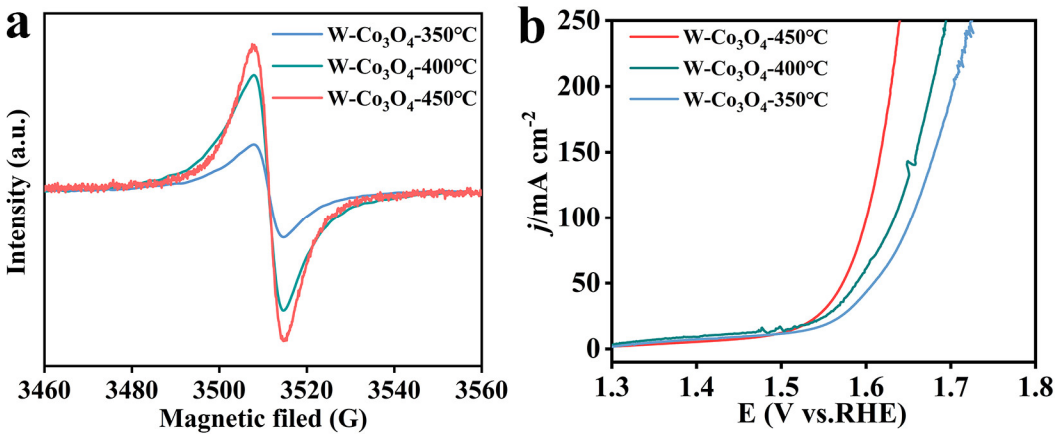

Figure S33. (a) EPR spectra of W-Co_3O_4 samples with various amounts of oxygen vacancies. (b) LSV curves of W-Co_3O_4 samples with various amounts of oxygen vacancies in 0.5 M H_2SO_4.

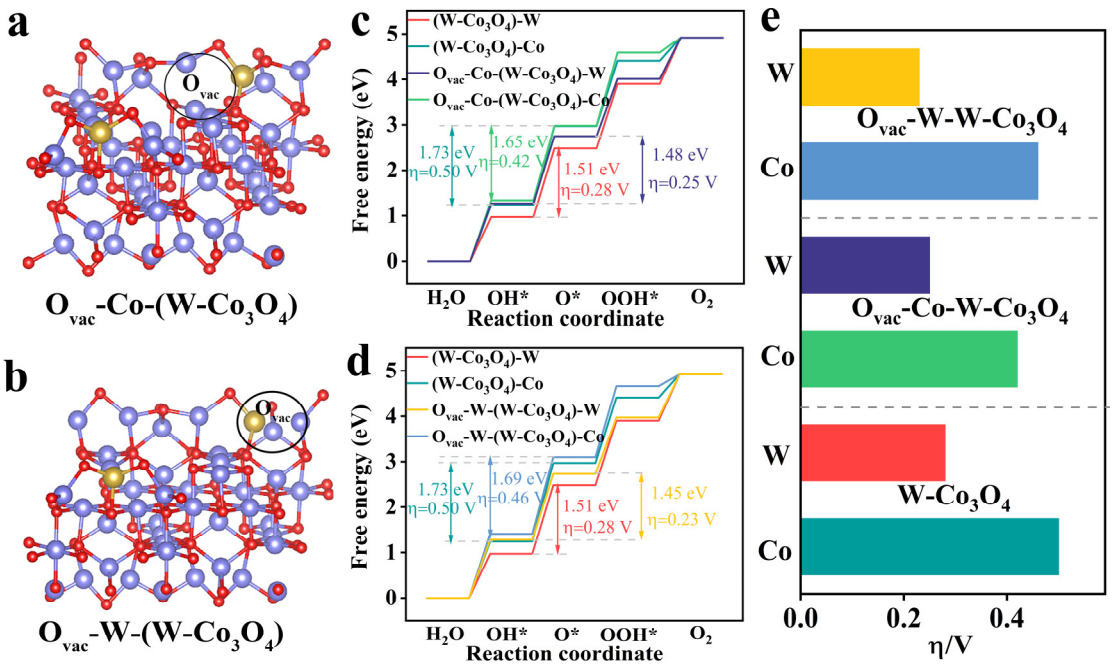

Figure S34. (a-b) DFT Calculated structures of (a) O_{vac}-Co-(W-Co_3O_4) and (b) O_{vac}-W-(W-Co_3O_4). (c-d) The reaction free energy diagrams of W and Co sites on W-Co_3O_4, O_{vac}-Co-(W-Co_3O_4), and O_{vac}-W-(W-Co_3O_4) for OER at 0 V vs. RHE by the AEM. (e) The overpotential determining step of W and Co sites on W-Co_3O_4, O_{vac}-Co-(W-Co_3O_4), and O_{vac}-W-(W-Co_3O_4).

To further confirm the effect of oxygen vacancies on the OER activity of W-Co_3O_4 in the above experiments, we then conducted a DFT calculation to explore the OER mechanism. Considering the possible location of oxygen vacancies, we constructed two oxygen vacancy models O_{vac}-Co-(W-Co_3O_4) and O_{vac}-W-(W-Co_3O_4) based on the model of W-Co_3O_4 in the neighborhood of Co and W, respectively. According to these two models, we calculated the Gibbs free energy for the OER reaction pathways at the W and Co sites, respectively. As shown in Figure R2-2c and 2d, the rate-limiting step occurs at the OH* intermediate to the O* intermediate. The results indicated the addition of oxygen vacancies did not change the rate-limiting step of W-Co_3O_4 for OER. In addition, as shown in Figures 34e, the overpotential determining step of W and Co sites on O_{vac}-Co-(W-Co_3O_4) and O_{vac}-W-(W-Co_3O_4) are lower than W-Co_3O_4. DFT results indicated that oxygen vacancies can optimize the adsorption energy of W, Co sites on W-Co_3O_4, lower the reaction barrier of the rate-limiting step, and improve the OER catalytic activity.

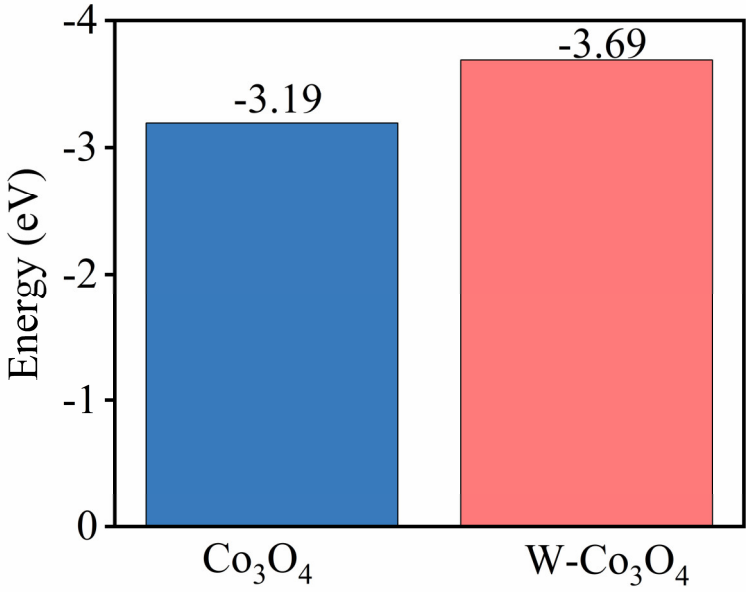

Figure S35. The O 2p band center at Co_3O_4 and W-Co_3O_4

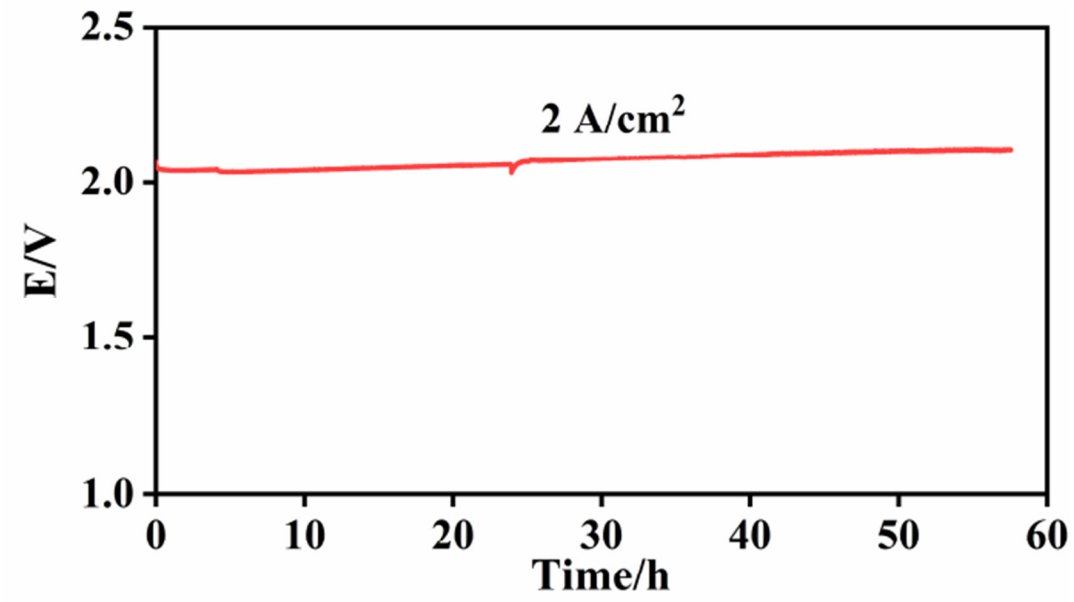

Figure S36. The Chronopotentiometry curve of the PEMWE using W-Co_3O_4 as an OER catalyst and commercial Pt/C as an HER catalyst (Pt loading: 0.8 mg cm^{-2}) at 2 A/cm^2 at 50 ℃ with Nafion 115 membrane.

Table S1. EXAFS fitting parameters at the Co K-edge for various samples

	shell	CN	R(Å)	σ^2	ΔE_0	R factor
Co foil	Co-Co	12	2.49±0.01	0.0076	6.6±1.0	0.0092
Co_3O_4	Co-O	5.3	1.85±0.01	0.0028	-8.5±0.5	0.0065
	Co-Co	4.0	2.80±0.01	0.0031		
	Co-Co	8.0	3.40±0.01	0.0084		
W-Co_3O_4	Co-O	5.0±0.4	1.87±0.01	0.0029	8.0±2.7	0.0110
	Co-Co	3.7±0.4	2.89±0.02	0.0029		
	Co-Co	5.1±0.9	3.37±0.03	0.0059		

CN: coordination numbers; *R*: bond distance; σ^2: Debye-Waller factors; ΔE_0: the inner potential correction. *R* factor: goodness of fit

Table S2. EXAFS fitting parameters at the W L_3-edge for various samples

	shell	CN	R(Å)	σ^2	ΔE_0	R factor
W foil	W-W	8	2.74±0.004	0.0027	6.42±1.43	0.0078
	W-W	6	3.17±0.004	0.0035		
WO_3	W-O	4.0±0.3	1.77±0.01	0.0024	7.1±1.1	0.0120
	W-O	1.9±0.5	2.17±0.02	0.0029		
W-Co_3O_4	W-O	2.80±0.47	1.78±0.016	0.0029	5.32±2.7	0.02

Table S3. Comparisons of the OER activity and stability of reported Co-based catalysts in acid.

Catalysts	Electrolyte	Activity (overpotential/mV)@10 mA/cm^2	Stability (hrs)	Reference
CeO_2/Co_3O_4	0.5 M H_2SO_4	410	50	*Nat. Commun.*[10]
$CoFePbO_x$	H_2SO_4 pH=1	450	24	*Nat. Catal.*[11]
Co_3O_4@C/GPO	1.0 M H_2SO_4	360	42.5	*Nat. Commun.*[12]
$Co_{3-x}Ba_xO_4$	0.5 M H_2SO_4	278	110	*JACS*[13]
Co_3O_4	0.5 M H_2SO_4	570	12	*Chem. Mater.*[14]
$Ir_{0.06}Co_{2.94}O_4$	0.1 M $HClO_4$	300	200	*JACS*[15]
Ag-Co_3O_4	0.5 M H_2SO_4	470	10	*JMCA*[16]
Ir-Co_3O_4	0.5 M H_2SO_4	236	30	*Nat. Commun.*[17]
$RuO_2/(Co,Mn)_3O_4$	0.5 M H_2SO_4	270	24	*Appl. Catal. B*[18]
Co_3O_4@C	0.5 M H_2SO_4	370	86.8	*Nano energy*[19]
Ru/RuO_2-Co_3O_4	0.1 M $HClO_4$	226	19	*ACS Energy Lett*[20]
IrCo NDs	0.1 M $HClO_4$	390	5.5	*ACS Appl. Mater. Interfaces*[21]
Ir-$NiCo_2O_4$ NSs	0.5 M H_2SO_4	240	70	*JACS*[22]
$Ta_xCo_{3-X}O_4$	0.5 M H2SO4	378	140	*Energy environ., Sci*[26]
W-Co_3O_4	**0.5 M H_2SO_4**	**251**	**250**	***This work***

Table S4. Adsorption free energy for OH*, O*, and OOH* on different surfaces

	G_{ad} OH*	G_{ad} O*	G_{ad} OOH*
Co_3O_4(311)-Co	0.70	2.66	4.27
W-Co_3O_4(311)-Co	1.24	2.97	4.41
W-Co_3O_4(311)-W	0.97	2.48	3.90

Table S5. OER stability of reported noble metal-free catalysts in PEMWE

Catalysts	Current mA/cm^2	Stability (hrs)	Reference
La,Mn-Co_3O_4 (LMCF)	210	100	*Science*[23]
Co_9S_8/Co_3O_4	50	24	*Angew. Chem. Int. Edit.*[24]
MnO_2	100	12	*Angew. Chem. Int. Edit*[1]
CoFeNiMoWTe	1000	100	*Adv. Energy. Matter*[25]
	100	**400**	
W-Co_3O_4	**250**	**310**	***This work***
	1000	**240**	

Reference

1. A. Li, H. Ooka, N. Bonnet, T. Hayashi, Y. Sun, Q. Jiang, C. Li, H. Han and R. Nakamura, *Angew. Chem.,Int. Edit.*, 2019, **58**, 5054-5058.
2. Y. Zhu, J. Wang, T. Koketsu, M. Kroschel, J.-M. Chen, S.-Y. Hsu, G. Henkelman, Z. Hu, P. Strasser and J. Ma, *Nat. Commun.*, 2022, **13**, 7754-7754.
3. A. B. Anderson, J. Roques, S. Mukerjee, V. S. Murthi, N. M. Markovic and V. Stamenkovic, *J. Phys. Chem. B.*, 2005, **109**, 1198-1203.
4. Y. Duan, N. Dubouis, J. Huang, D. A. Dalla Corte, V. Pimenta, Z. J. Xu and A. Grimaud, *ACS Catal.*, 2020, **10**, 4160-4170.
5. J. Huang, H. Sheng, R. D. Ross, J. Han, X. Wang, B. Song and S. Jin, *Nat. Commun.*, 2021, **12**, 3036.
6. G. Kresse and J. Furthmuller, *Computational Materials Science*, 1996, **6**, 15-50.
7. G. Kresse and J. Furthmuller, *Phys. Rev. B.*, 1996, **54**, 11169-11186.
8. J. P. Perdew, K. Burke and M. Ernzerhof, *Phys.l Rev. Lett.*, 1997, **78**, 1396-1396.
9. I. C. Man, H.-Y. Su, F. Calle-Vallejo, H. A. Hansen, J. I. Martinez, N. G. Inoglu, J. Kitchin, T. F. Jaramillo, J. K. Norskov and J. Rossmeisl, *Chemcatchem*, 2011, **3**, 1159-1165.
10. J. Z. Huang, H. Y. Sheng, R. D. Ross, J. C. Han, X. J. Wang, B. Song and S. Jin, *Nat. Commun.*, 2021, **12**, 3036.
11. M. Chatti, J. L. Gardiner, M. Fournier, B. Johannessen, T. Williams, T. R. Gengenbach, N. Pai, N. Cuong, D. R. MacFarlane, R. K. Hocking and A. N. Simonov, *Nat. Catal.*, 2019, **2**, 457-465.
12. J. Yu, F. A. Garces Pineda, J. Gonzalez Cobos, M. Pena-Diaz, C. Rogero, S. Gimenez, M. Chiara Spadaro, J. Arbiol, S. Barja and J. Ramon Galan Mascaros, *Nat. Commun.*, 2022, **13**, 4341.
13. N. Wang, P. Ou, R. K. Miao, Y. Chang, Z. Wang, S.-F. Hung, J. Abed, A. Ozden, H.-Y. Chen, H.-L. Wu, J. E. Huang, D. Zhou, W. Ni, L. Fan, Y. Yan, T. Peng, D. Sinton, Y. Liu, H. Liang and E. H. Sargent, *J. Am. Chem. Soc.*, 2023, **145**, 7829-7836.
14. J. S. Mondschein, J. F. Callejas, C. G. Read, J. Y. C. Chen, C. F. Holder, C. K. Badding and R. E. Schaak, *Chem. Mater.*, 2017, **29**, 950-957.
15. J. Shan, C. Ye, S. Chen, T. Sun, Y. Jiao, L. Liu, C. Zhu, L. Song, Y. Han, M. Jaroniec, Y. Zhu, Y. Zheng and S.Z. Qiao, *J. Am. Chem. Soc.*, 2021, **143**, 5201-5211.

16. K.-L. Yan, J.-Q. Chi, J.-Y. Xie, B. Dong, Z.-Z. Liu, W.-K. Gao, J.-H. Lin, Y.-M. Chai and C.-G. Liu, *Renewable Energy*, 2018, **119**, 54-61.
17. Y. Zhu, J. Wang, T. Koketsu, M. Kroschel, J. M. Chen, S. Y. Hsu, G. Henkelman, Z. Hu, P. Strasser and J. Ma, *Nat. Commun.*, 2022, **13**, 7754.
18. S. Niu, X.-P. Kong, S. Li, Y. Zhang, J. Wu, W. Zhao and P. Xu, *Appl. Catal. B: Environ.*, 2021, **297**, 120442.
19. X. Yang, H. Li, A.-Y. Lu, S. Min, Z. Idriss, M. N. Hedhili, K.-W. Huang, H. Idriss and L. J. Li, *Nano Energy*, 2016, **25**, 42-50.
20. T. Wang, Z. Li, H. Jang, M. G. Kim, Q. Qin and X. Liu, *ACS Sustain. Chem & Eng.*, 2023, **11**, 5155-5163.
21. L. Fu, X. Zeng, G. Cheng and W. Luo, *ACS Appl. Mater. Interfaces*, 2018, **10**, 24993-24998.
22. J. Yin, J. Jin, M. Lu, B. Huang, H. Zhang, Y. Peng, P. Xi and C.H. Yan, *J. Am. Chem. Soc.*, 2020, **142**, 18378-18386.
23. L. Chong, G. Gao, J. Wen, H. Li, H. Xu, Z. Green, J. D. Sugar, A. J. Kropf, W. Xu, X. M. Lin, H. Xu, L. W. Wang and D. J. Liu, *Science*, 2023, **380**, 609-616.
24. L. Wang, H. Su, Z. Zhang, J. Xin, H. Liu, X. Wang, C. Yang, X. Liang, S. Wang, H. Liu, Y. Yin, T. Zhang, Y. Tian, Y. Li, Q. Liu, X. Sun, J. Sun, D. Wang and Y. Li, *Angew. Chem., Int. Edit.*, 2023, e202314185.
25. S. Jo, M.C. Kim, K. B. Lee, H. Choi, L. Zhang and J. I. Sohn, *Adv.Energy Mater.*, 2023, **13**, 2301420.
26. K. Lee, J. Shim, H. Ji, J. Kim, H. S. Lee, H. Shin, M. S. Bootharaju, K. S. Lee, W. Ko, J. Lee, K. Kim, S. Yoo, S. Heo, J. Ryu, S. Back, B. H. Lee, Y. E. Sung and T. Hyeon, Energy Environ. Sci., 2024, 17, 3618-3628.